AGU PUBLICATIONS

Space Weather

RESEARCH ARTICLE
10.1002/2016SW001375

Special Section:
Reprise of "Space Weather" 2001 Monograph

On the origins and timescales of geoeffective IMF

Mike Lockwood[1], Mathew J. Owens[1], Luke A. Barnard[1], Sarah Bentley[1], Chris J. Scott[1], and Clare E. Watt[1]

[1]Department of Meteorology, University of Reading, Reading, UK

Abstract Southward interplanetary magnetic field (IMF) in the geocentric solar magnetospheric (GSM) reference frame is the key element that controls the level of space weather disturbance in Earth's magnetosphere, ionosphere, and thermosphere. We discuss the relation of this geoeffective IMF component to the IMF in the geocentric solar ecliptic (GSE) frame, and using the almost continuous interplanetary data for 1996–2015 (inclusive), we show that large geomagnetic storms are always associated with strong southward, out-of-ecliptic field in the GSE frame: Dipole tilt effects, which cause the difference between the southward field in the GSM and GSE frames, generally make only a minor contribution to these strongest storms. The time-of-day/time-of-year response patterns of geomagnetic indices and the optimum solar wind coupling function are both influenced by the timescale of the index response. We also study the occurrence spectrum of large out-of-ecliptic field and show that for 1 h averages it is, surprisingly, almost identical in ICMEs (interplanetary coronal mass ejections), around CIRs/SIRs (corotating and stream interaction regions) and in the "quiet" solar wind (which is shown to be consistent with the effect of weak SIRs). However, differences emerge when the timescale over which the field remains southward is considered: for longer averaging timescales the spectrum is broader inside ICMEs, showing that these events generate longer intervals of strongly southward average IMF and consequently stronger geomagnetic storms. The behavior of out-of-ecliptic field with timescale is shown to be very similar to that of deviations from the predicted Parker spiral orientation, suggesting the two share common origins.

Key Points:
- The roles of out-of-ecliptic field and Earth's dipole tilt in generating storms of various intensities are quantified
- Small-scale solar wind structure and CIRs generate as many hours of strong southward IMF as ICMEs
- Persistence of strong southward IMF explains response patterns and why ICMEs are more geoeffective

Correspondence to:
M. Lockwood,
m.lockwood@reading.a.uk

Citation:
Lockwood, M., M. J. Owens, L. A. Barnard, S. Bentley, C. J. Scott, and C. E. Watt (2016), On the origins and timescales of geoeffective IMF, *Space Weather*, *14*, 406–432, doi:10.1002/2016SW001375.

Received 9 FEB 2016
Accepted 24 MAY 2016
Accepted article online 2 JUN 2016
Published online 24 JUN 2016

1. Introduction

Magnetic reconnection in the dayside magnetopause current sheet, at latitudes between Earth's magnetic cusps, was first proposed by *Dungey* [1961] to explain ionospheric currents. Subsequently, it has been shown to be the dominant driver of magnetospheric structure, dynamics, currents, and plasma populations. As well as providing direct access for solar wind particles to enter the magnetosphere [*Cowley*, 1982; *Smith and Lockwood*, 1996; *Lockwood and Davis*, 1996] and directly driving flows and currents in the dayside ionosphere [*Nishida*, 1968; *Etemadi et al.*, 1988; *Todd et al.*, 1988; *Cowley and Lockwood*, 1992] (both effects involved in the generation of polar patches in the ionospheric *F* region, features that have space weather implications [*Zhang et al.*, 2013, 2015]), these open field lines are swept into the geomagnetic tail by the solar wind flow, where energy is stored in the form of the increased Maxwell magnetic pressure, increasing the current in the near-Earth cross-tail current sheet and expanding the diameter of the far tail. This energy is released (and the near-Earth cross-tail current disrupted into the ionosphere in the "current wedge") during substorm expansion phases [*McPherron et al.*, 1973], causing bursts of energy, momentum, and particle deposition into even the innermost near-Earth magnetosphere [*Konradi et al.*, 1975; *Reeves et al.*, 2003; *Turner et al.*, 2015] and perturbations to the thermosphere that propagate round the globe [*Fujiwara et al.*, 1996; *McGranaghan et al.*, 2014]. The flow of solar wind energy into and through the coupled magnetosphere-ionosphere-thermosphere system was described using Poynting's theorem by *Cowley* [1991] for steady state. This was generalized for each substorm phase separately by *Lockwood* [2004]. Because Earth presents a northward pointing magnetic field to the solar wind flow at latitudes between the magnetic cusps, these phenomena, and their associated space weather effects, are all enhanced when the interplanetary magnetic field (IMF) has a southward orientation, such that there is large magnetic shear across the low-latitude dayside magnetopause: This allows the rapid opening of the geomagnetic field lines by magnetic reconnection. Thus, in order to accurately predict space weather disturbances, it is necessary to predict the southward component of the IMF in a suitable reference frame, oriented by Earth's magnetic field such that it quantifies the magnetic shear across the dayside, low-latitude magnetopause. The geocentric solar magnetospheric (GSM) coordinate system [*Hapgood*, 1992] is the most commonly used and successful reference frame in this context.

In this paper, we investigate the nature of "geoeffective" IMF orientations, i.e., those which cause space weather disturbances in the terrestrial magnetosphere-ionosphere-thermosphere system and, in particular, geomagnetic activity. We use near-continuous observations spanning nearly two solar cycles (1996–2015) to study the interplay between, and relative influence of, geometric factors (associated with time of day (universal time, UT) and time of year because of the tilt in the Earth's magnetic dipole axis or Earth's heliographic latitude—see section 2.1) and the IMF associated with large solar wind disturbances (section 2.2) and small-scale structure (section 2.4), with particular emphasis on the effect of timescales (section 2.3). It is well known that there is a semiannual variation in average geomagnetic activity and that this variation is also seen in the occurrence of the largest disturbances ("great storms"), with significantly more occurring around the equinoxes than around the solstices. However, it is not clear that this annual variation in the occurrence of great storms has the same combination of causes as the seemingly similar annual variation in average geomagnetic activity levels [e.g., *Crooker et al*., 1992; *Svalgaard et al*., 2002]. Hence, in our analysis (section 3) we also study how the contributions of different factors vary with the level of geomagnetic disturbance and, in particular, the importance of out-of-ecliptic IMF, relative to the effect of in-ecliptic IMF combined with the geometric effects caused by Earth's dipole tilt. Section 4 studies the spectrum of the out-of-ecliptic IMF component, how it is influenced by timescale, and how it relates to deviations from the Parker spiral orientation of the IMF. Our conclusions are summarized in section 5.

2. Influences on Terrestrial Space Weather

2.1. Geometric Factors

Figure 1 defines the GSM and the geocentric solar ecliptic (GSE) coordinate systems [*Hapgood*, 1992] and explains why the angle between the Z_{GSE} and Z_{GSM} axes, $(\delta_a + \delta_d)$ has both annual and diurnal periodicities. We define the angles giving these annual and diurnal variations (respectively, δ_a and δ_d) as both being positive in the clockwise direction when Earth is viewed from the Sun. The difference between the GSM and GSE frames gives rise to the Russell-McPherron (R-M) effect: This is a geometric effect whereby in-ecliptic field in the $\pm Y_{GSE}$ direction causes a $\pm Z_{GSM}$ field component [*Russell and McPherron*, 1973]. This is significant for steady and uniform solar wind flow because the application of the ideal-MHD, frozen-in theorem in Parker spiral theory predicts a near-Earth IMF that lies in a plane close to the ecliptic, [e.g., *Owens and Forsyth*, 2013] and this gives, on average, a near-Earth IMF with $B_Z(\mathrm{GSE}) \approx 0$ and large $|B_Y(\mathrm{GSE})|$ [*Hapgood et al*., 1991]. Figure 1 shows how, because $\sin(\delta_a + \delta_d) > 0$ around the March equinox, $B_Y(\mathrm{GSE}) < 0$ gives rise to southward IMF in the GSM frame ($B_Z(\mathrm{GSM}) < 0$), particularly at 22 UT when $(\delta_a + \delta_d)$ reaches a maximum value of 34.5°. Note that at this time $B_Y(\mathrm{GSE}) > 0$ gives rise to northward IMF in the GSM frame ($B_Z(\mathrm{GSM}) > 0$). Conversely, around the September equinox when $\sin(\delta_a + \delta_d) < 0$, it is $B_Y(\mathrm{GSE}) > 0$ that gives rise to southward IMF in the GSM frame (and $B_Y(\mathrm{GSE}) < 0$ gives $B_Z(\mathrm{GSM}) > 0$): This is especially true at 10UT when $(\delta_a + \delta_d)$ has a minimum value of $-34.5°$. The precise dates of the extremes in δ_a (the equinoxes) drift slowly: for 2015 they were 20 March and 22 September. The R-M effect correctly predicts that geomagnetic activity will peak near the equinoxes, but note that averaged magnetic indices do not show the precise time-of-day/time-of-year (t-o-d/t-o-y) pattern predicted for the R-M effect [*Cliver et al*., 2000; *Finch et al*., 2008]. Instead, several such indices give a t-o-d/t-o-y pattern that has been termed "equinoctial" which indicates that the tilt of the Earth's rotational and/or magnetic axes toward or away from the Sun also has an influence, introducing differences between the two solstices and between 4 UT and 16 UT which are not predicted by the R-M effect [*O'Brien and McPherron*, 2002].

The predicted t-o-d/t-o-y pattern for the R-M effect is plotted in Figure 2a which shows color contours of $|\sin(\delta_a + \delta_d)|$ (see Figure 1) as a function of fraction of the year, f_{year}, (horizontal axis, where $f_{year} = 0$ at the start of 1 January and $f_{year} = 1$ at the end of 31 December) and universal time (UT, vertical axis). The modulus $|\sin(\delta_a + \delta_d)|$ is plotted because it can reflect the effect of the either polarity of IMF $B_Y(\mathrm{GSE})$ (whichever is the relevant one at that t-o-y) in generating $B_Z(\mathrm{GSM}) < 0$. Figure 2d shows fitted contours on the same axes of the mean observed southward IMF in GSM coordinates, $B_S(\mathrm{GSM})$ (where $B_S(\mathrm{GSM}) = -B_Z(\mathrm{GSM})$ when $B_Z(\mathrm{GSM}) < 0$ and $B_S(\mathrm{GSM}) = 0$ when $B_Z(\mathrm{GSM}) \geq 0$) for all IMF data available (1963–2015). This clearly reveals the R-M pattern [see also *O'Brien and McPherron*, 2002].

Figure 2b demonstrates the equinoctial pattern by showing $\cos(\psi)$ on the same axes, where ψ is the full angle, in three dimensions, between the Earth's magnetic dipole axis, $\vec{M}$ and the GSE X axis [see *O'Brien*

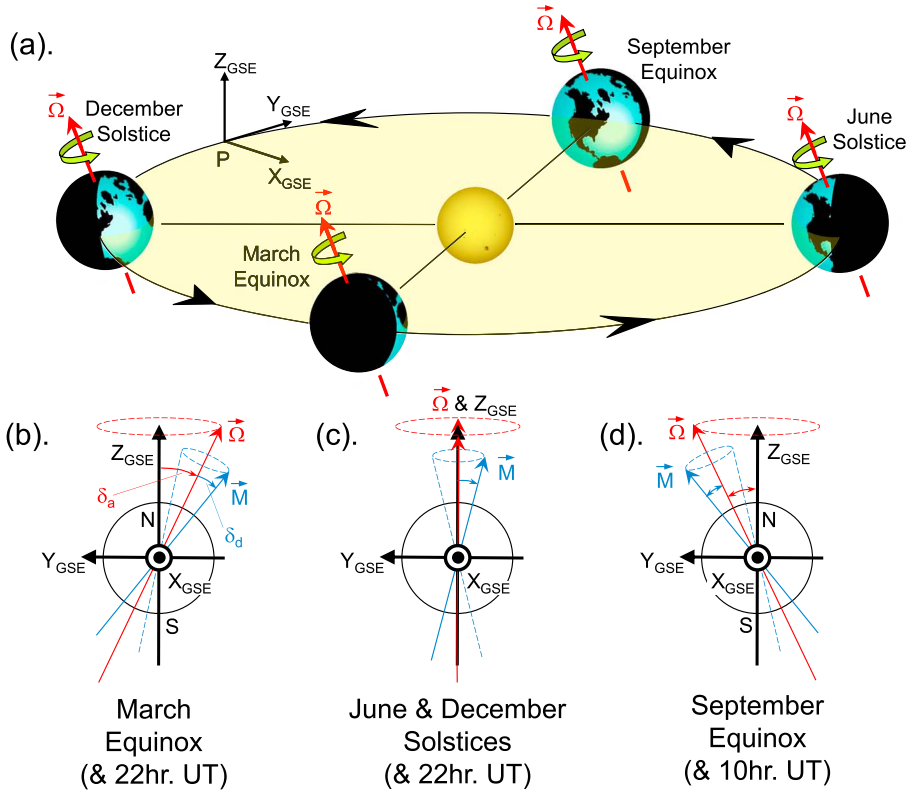

Figure 1. (a) Earth's orbit and the orientation of its rotational axis, $\vec{\Omega}$ (in red). The *X*, *Y*, and *Z* axes of the geocentric solar ecliptic (GSE) coordinate system are illustrated here for the time when the Earth's center is at the point *P* (between the September equinox and the December solstice). (b–d) The Earth viewed from the Sun for the March equinox, the June or December solstices, and the September equinox, respectively: In addition to showing $\vec{\Omega}$ (in red), each panel shows the Earth's magnetic axis, $\vec{M}$ (in blue), both projected onto the *Z-Y* plane of the GSE frame. (b and c) $\vec{M}$ is shown for 22 UT and for 10 UT in (d). By definition, the *X* axis of the geocentric solar magnetospheric (GSM) frame is the same as for GSE (i.e., toward the Sun), and the Z_{GSM} axis is aligned with the projection of $\vec{M}$ onto the *Z-Y* plane of the GSE frame. As illustrated in Figure 1a, Earth's orbital motion causes $\vec{\Omega}$ to gyrate annually around the Z_{GSE} axis at an angle of 23.5°, while its rotation and offset of magnetic and rotation poles causes $\vec{M}$ to gyrate daily around $\vec{M}$ at an angle of 11°. The angle δ_a varies between +23.5° at the March equinox and −23.5° at the September equinox and δ_d varies between +11° at 22 UT and −11° at 10 UT. (Both angles being defined as positive clockwise, as seen from the Sun) The total angle between the Z_{GSE} and Z_{GSM} axes is $(\delta_a + \delta_d)$.

and McPherron, 2002]. Figure 2e shows mean values of the a_m index (for 1959–2015) which, while not exactly replicating the pattern in Figure 2b, is nevertheless very similar in character. Note that a_m is a 3-hourly "range" index (i.e., based on the range of variation in each 3 h interval) compiled from a network of stations between geographic latitudes of 50°S and 50°N, currently with 11 in the northern hemisphere and 10 in the southern. The UT resolution is therefore limited to just 8 data points per day and the distribution of stations with longitude in each hemisphere is not ideal which introduces some spurious UT variation. There have been a number of plausible explanations proposed for this observed equinoctial pattern. These include the following: Tilt-induced changes in the ionospheric conductivity within the nightside auroral electrojet of the substorm current wedge [*Lyatsky et al*., 2001]; tilt influence on the magnetopause reconnection voltage [*Russell et al*., 2003; *Crooker and Siscoe*, 1986]; the effect of tilt on the proximity of the ring current and auroral electrojet [*Alexeev et al*., 1996]; and tilt effects on the stability of the cross-tail current sheet. The last of these possibilities arises because the dipole-tilt-oriented structure in the near-Earth magnetosphere turns into the solar-wind-aligned far tail as one moves antisunward down the tail: The "hinge" between the two regimes has a UT variation and occurs at a (negative) *X* value close to where the cross-tail current is disrupted during substorm expansion phases [*Kivelson and Hughes*, 1990; *Miyashita et al*., 2009]. *Finch et al.* [2008] used a global network of geomagnetic stations to show that the equinoctial behavior originates during substorm expansion phases and in the substorm current wedge and is not a feature of dayside currents and flows during the substorm

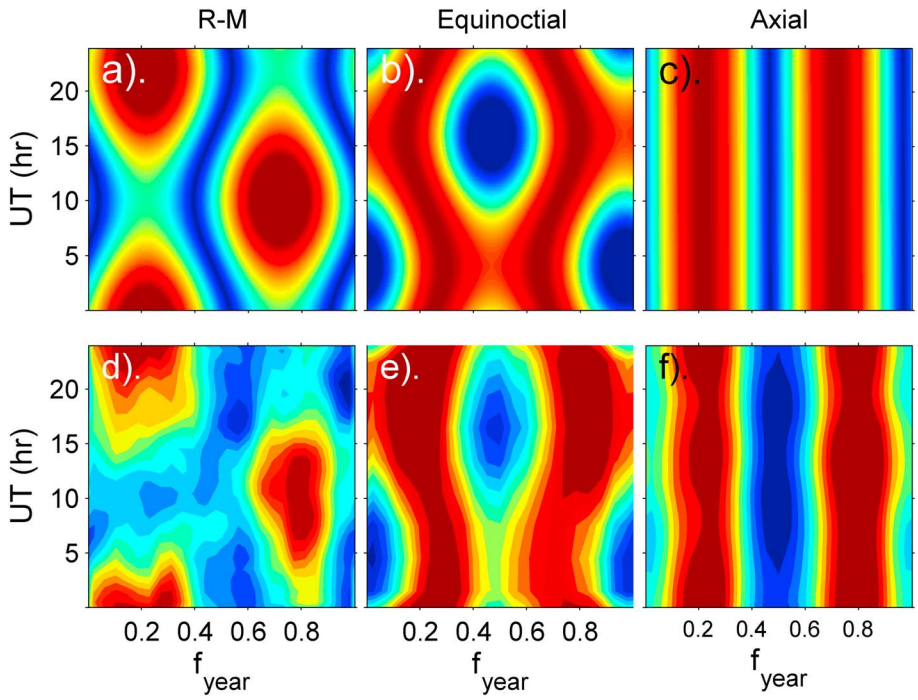

Figure 2. Predicted and observed time-of-day/time-of-year patterns. (a–c) Predictions based on geometric factors and (d–f) the contoured patterns in means of observations. (Figure 2a) the Russell-McPherron (R-M) pattern: The filled color contours show $|\sin(\delta_a + \delta_d)|$ (see Figure 1) as a function of fraction of the year, f_{year}, (horizontal axis) and UT (vertical axis). (Figure 2b) The equinoctial pattern, shown by $\cos(\psi)$ where ψ is the full angle between the Earth's magnetic dipole axis, $\bar{M}$, and the GSE X axis. (Figure 2c) An axial pattern shown by $|\sin(\Lambda_E)|$, where Λ_E is the heliographic latitude of Earth. (Figure 2d) The pattern for the mean of the observed southward IMF in GSM coordinates, B_S(GSM), where $B_S(\mathrm{GSM}) = -B_Z(\mathrm{GSM})$ when $B_Z(\mathrm{GSM}) < 0$ and $B_S(\mathrm{GSM}) = 0$ when $B_Z(\mathrm{GSM}) \geq 0$. (Figure 2e) The pattern for the a_m geomagnetic index. (Figure 2f) The pattern for $-k(\mathrm{UT}) \times Dst$ where the factor k(UT) is the modeled response of the four *Dst* stations that allows for the fact that they are not equally spaced in longitude (see section 3.1 of text). To get good coverage, all available data were used in each case, namely, 1963–2015 for the IMF data in Figure 2d; 1959–2015 for the a_m data in Figure 2e; and 1957–2015 for the *Dst* data in Figure 2f. In all cases we are concerned only with the form of the pattern rather than the amplitude and color scales have been autoscaled between the maximum and minimum values.

growth phase. (These authors showed that the dayside currents do not depend on UT and vary only with season, being greater in summer when conductivities are higher.) These results by Finch et al. therefore strongly support the explanations of the equinoctial effect invoking nightside magnetospheric or ionospheric effects rather than those that postulate modulation of the magnetopause reconnection voltage. Note also that indices influenced by the substorm current wedge also depend on the solar wind dynamic pressure P_{SW} ($= m_{SW} N_{SW} V_{SW}^2$, where m_{SW} is the mean ion mass, N_{SW} is the ion number density, and V_{SW} is the speed of the solar wind), because it compresses the near-Earth geomagnetic tail and so modulates the near-Earth cross-tail current there for a given open flux content in the tail [*Lockwood*, 2013]. There has been considerable debate about the effect of P_{SW} and hence of the solar wind concentration N_{SW}, on the *Dst* geomagnetic index. This debate has been reviewed by *Weigel* [2010], who also finds that a given southward IMF is more "geoeffective" (meaning that it has more effect on the terrestrial space environment) if P_{SW} and N_{SW} is higher (but no effect of the solar wind speed, V_{SW}, nor of the mean solar wind ion mass, m_{SW}, was found). This is most consistent with the idea of enhanced N_{SW} "preconditioning" the magnetosphere (by generating a dense plasma sheet), discussed below in section 2.2. From a superposed epoch study, *Zhang et al.* [2006] find almost no difference between the behavior of the mean half-wave rectified southward IMF, B_S(GSM), and the mean eastward electric field, $E_Y(\mathrm{GSM}) = V_{SW} \times B_S(\mathrm{GSM})$ in the interplanetary drivers for moderate and intense storms which also points to V_{SW} having no specific effect, other than via the compression and orientation change of the IMF [*Kane*, 2005]. Note that *Balan et al.* [2015] find that the rise in solar wind speed, ΔV_{SW}, associated with the impact of an interplanetary coronal mass ejection (ICME) does have a direct effect on the magnitude of the subsequent storm. This finding is not inconsistent with the

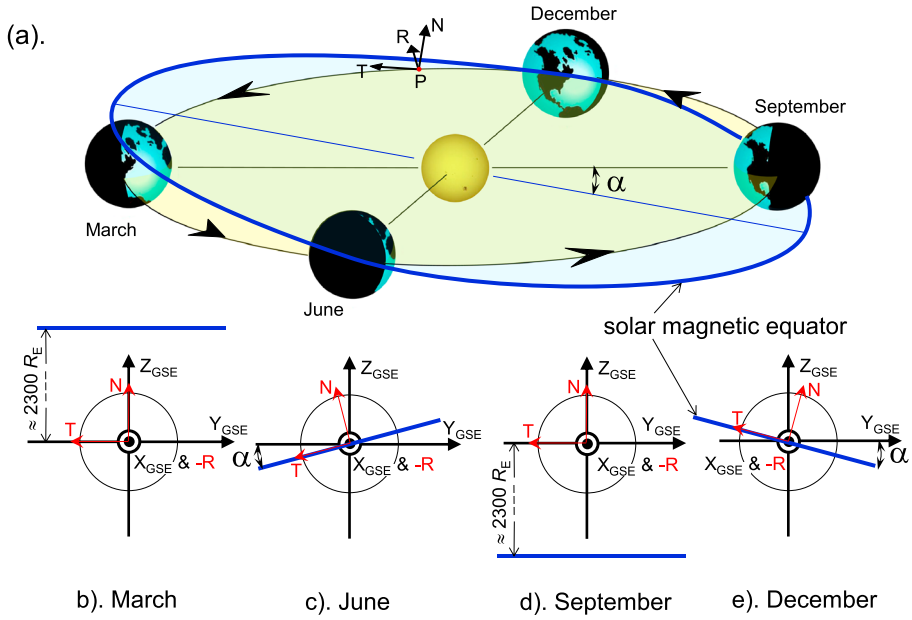

Figure 3. (a) The axial effect. The solar equatorial plane (shaded light blue) is inclined by $\alpha \approx 7°$ with respect to the ecliptic plane (shaded pale yellow) such that in March, Earth lies in the southern solar hemisphere and in September it lies in the northern solar hemisphere. The *R*, *T*, and *N* axes of the heliocentric RTN coordinate system are illustrated here for when the Earth's center is at the point *P* (between December and March). *R* is the radial direction and so antiparallel to X_{GSE} (and hence also to X_{GSM}), the *T* direction is the perpendicular to *R* that lies in the plane parallel to the solar magnetic equator (and has a positive component in the $-Y_{GSE}$ direction), and the *N* is the northward direction of increasing heliographic latitude. For a Parker spiral configuration, the field has *T* and *R* components but the *N* component is zero. (b–e) The Earth viewed from the Sun in March, June, September, and December, respectively.

studies showing no effect of V_{SW} (or the work presented here) because larger ΔV_{SW} will give larger out-of-ecliptic field in the ICME sheath region which will generally add to the integrated southward IMF that impacts upon Earth's magnetic field [*Owens et al.*, 2005].

The R-M effect is not the only way that geometric factors can influence the B_Z(GSM) component. Figure 3a illustrates effects arising because the solar equatorial plane (normal to the solar rotation axis) is inclined at an angle $\alpha \approx 7°$ with respect to the ecliptic, such that Earth makes a maximum southward deviation from the solar equator on 6 March and a maximum deviation to the north on 7 September. The effects of this have been termed "axial," and depend on t-o-y (f_{year}) but not on t-o-d (UT), as shown in Figure 2c which plots the t-o-d/t-o-y pattern of $|\sin(\Lambda_E)|$, where Λ_E is the heliographic latitude of Earth. When $|\sin(\Lambda_E)|$ is larger, Earth's magnetosphere is more likely to be embedded in fast solar wind, outside the streamer belt [*Lockwood and Owens*, 2014], particularly at sunspot minimum when the streamer belt is thinnest [*Owens et al.*, 2014]. In addition, near-Earth space at such times is more likely to be threaded by solar polar field lines and so have an excess of toward ($B_x > 0$) or away ($B_x < 0$) heliospheric magnetic field, depending on the t-o-y and the prevailing polarity of the solar polar fields (and hence on the phase of the 22 year Hale cycle). This is called the Rosenberg-Coleman (R-C) effect [*Rosenberg and Coleman*, 1969]. Because the field usually obeys a Parker spiral configuration [*Parker*, 1958], the annual cycle of bias in B_X caused by the R-C effect is associated with corresponding bias in the B_Y(GSE) component and hence, by the R-M effect, also induces a bias in B_Z (GSM). This is often called the combined R-C/R-M effect.

In addition, there is a second annual geometric effect associated with the variable difference between the GSE and heliocentric RTN reference frames (where the *R* axis is radially away from the Sun, the *N* axis is the northward direction of increasing heliographic latitude, and the *T* axis is the tangential direction that makes up the right-hand set and lies in the plane parallel to the solar equator, as shown in Figure 3). This effect must be considered, for example, when transforming predictions of global MHD models of the heliosphere (such as Enlil [*Odstrcil et al.*, 2004a, 2004b]), which generally use RTN coordinates, into the GSE frame. For uniform solar source magnetic field and uniform and constant solar wind flow speed, the heliospheric

field will form a Parker spiral configuration [*Parker*, 1958] with B_R and B_T components but for which B_N is always zero [*Owens and Forsyth*, 2013]. At the extremes of the Earth's motion around the solar equator (in March and September, as shown in Figures 3b and 3d) the Z_{GSE} and N directions are aligned, giving B_z (GSE) = 0 for a Parker spiral field configuration. However, in June and December the N direction is inclined to Z_{GSE} by an angle that peaks in magnitude at $\alpha \approx \pm 7°$ (as shown in Figures 3c and 3e). This means that around the June solstice a $B_T > 0$ component of the Parker spiral field (which occurs when $B_R < 0$, i.e., a "toward" IMF sector) yields $B_z(\mathrm{GSE}) < 0$, as shown in Figure 3c, whereas around the December solstice a $B_T < 0$ component (which, for a Parker spiral field, occurs when $B_R > 0$, i.e., an "away" IMF sector) yields $B_z(\mathrm{GSE}) < 0$, as shown in Figure 3e. Because this effect is a rotation by up to $\alpha = 7°$, compared to a peak value for $|\delta_a + \delta_d|$ of 34.5°, it is a smaller effect than the R-M effect and because it peaks near the solstices it is close to $\pi/2$ out of phase with the R-M effect.

2.2. Out-of-Ecliptic IMF and Transient Events

Persistent out-of-ecliptic IMF is typically found inside and ahead of transient events and fast-slow stream interaction regions. The most prominent transients are large-scale interplanetary coronal mass ejections (ICMEs) [*Webb and Howard*, 1994; *Cane and Richardson*, 2003; *Richardson and Cane*, 2010]. Roughly half of all ICMEs have embedded within them a magnetic flux-rope-like structure called a "magnetic cloud" (MC) [*Burlaga et al*., 1981; *Bothmer and Schwenn*, 1998]. MCs show either a bipolar or a unipolar variation in their north-south magnetic field component depending on their axis orientation with respect to the ecliptic plane [*Bothmer and Schwenn*, 1998; *Mulligan et al*., 1998]. When the orientation of the MC main axis has a significant in-ecliptic component, they give a bipolar structure of northward out-of-ecliptic IMF followed by southward or vice versa. If, on the other hand, the MC axis is highly inclined with respect to the ecliptic plane the field is either northward or southward during the whole passage of the MC with out-of-the ecliptic field maximizing at the axis [e.g. *Mulligan et al*., 1998; *Kilpua et al*., 2012]. Because of these southward fields (either in bipolar clouds or in so-called S-type unipolar clouds) they induce large terrestrial space weather disturbances and so ICMEs containing MCs are generally geoeffective. In addition, ahead of super-Alfvénic ejecta is an interplanetary shock front, behind which the perturbed IMF is draped over the event core in a sheath region: Here the preexisting IMF is enhanced and usually deflected northward or southward [*McComas et al*., 1989; *Gosling et al*., 1991; *Gonzalez et al*., 1999; *Huttunen et al*., 2002; *Jones et al*., 2002; *Owens et al*., 2005]. ICMEs are frequently seen at sector boundaries between toward ($B_X > 0$) and away ($B_X < 0$) IMF [e.g., *Owens and Forsyth*, 2013], especially at sunspot minimum [*Crooker et al*., 1998]. Roughly half of all ICMEs contain a definable MC, and these are the events that are generally found to be the most geoeffective [*Gosling*, 1993; *Richardson et al*., 2001, 2002]. Note also that identified MCs are also probably the largest events in a spectrum of flux-rope-associated solar ejections seen in interplanetary space [*Moldwin et al*., 2000; *Sheeley et al*., 2009; *Rouillard et al*., 2010a, 2010b, 2011].

Similarly in corotating interaction regions (CIRs), caused by fast solar wind emanating from coronal holes catching up slow solar wind ahead of it [*Smith and Wolfe*, 1976; *Pizzo*, 1978], the field is usually deflected out of the ecliptic plane as well as being enhanced by compression [*Gosling and Pizzo*, 1999]. Typically, hourly means of the magnetic field in CIR events are enhanced to 10–15 nT but they can reach 30 nT [*Gonzalez et al*., 1999]. The degree of compression and the out-of-ecliptic field component varies with the velocity difference between the fast and slow solar winds and the latitudinal extent of the CIR, the latter set by the latitudinal extent of the coronal hole boundary variation [e.g., *Rouillard and Lockwood*, 2007] which varies with the phase of the solar cycle. If the coronal hole source of the fast wind persists for several solar rotations at the same heliographic latitude as the source of slow solar wind, the CIR (which maps to the leading edge of the coronal hole) usually generates recurrent geomagnetic disturbances [*Crooker and Cliver*, 1994; *Rouillard and Lockwood*, 2007]. The heliospheric current sheet (HCS) that separates IMF sectors is often embedded within a CIR [*Gosling and Pizzo*, 1999]: Seemingly, this is because, as the forward Alfvén wave/shock propagates into the slow solar wind ahead, it overtakes and entrains the sector boundary, making it more likely for the HCS to be embedded within a CIR at larger distances from the Sun [*Thomas and Smith*, 1981]. Thus, CIRs, like ICMEs, often coincide with sector boundaries. Note that in some cases the source of the fast solar wind may be rapidly moving or may be short lived, in which case the interaction region ahead of them may not be seen to be corotating. These are referred to as "stream interaction regions" (SIRs).

The geoeffectiveness and occurrence of interplanetary shocks, MCs, non-MC ICMEs, CIRs, SIRs, and sector boundary crossings has been studied by many authors, often by looking at the response in the *Dst* geomagnetic index [e.g., *Yermolaev et al*., 2012], and events are often more geoeffective when they occur in combination [*Echer and Gonzalez*, 2004]. Ahead of both ICMEs and CIRs, containing both fast solar wind driver plasma and southward IMF, there is a tendency for there to be an interval of northward IMF, which has been proposed to precondition the magnetosphere and may make the subsequent transient more geoeffective [*Lavraud et al*., 2006; *Borovsky and Denton*, 2006]. The concept is that a denser (and colder) plasma sheet may form during the prior northward IMF, and this would lead to a stronger ring current when that plasma is convected inward during the main phase of an ensuing storm. *Borovsky et al.* [1998] found that there is a correlation between enhanced solar wind concentration N_{SW} and a denser plasma sheet; hence, northward IMF with enhanced N_{SW} would be the ideal preconditioning conditions. On the other hand, *Xie et al.* [2008] did not find any evidence that preconditioning was a factor in the intensity of large storms (although it does influence their duration), but they did find evidence for an effect of enhanced solar wind dynamic pressure P_{SW} during transient events. CIRs generate so-called high-speed stream storms [e.g., *Jordanova et al*., 2012; *Borovsky and Denton*, 2010] which may, in several respects, be somewhat underestimated in the response in *Dst*. Even so, *Kozyra et al.* [2006] and *Turner et al.* [2009] show that CIRs often give surprisingly large geomagnetic storms, given that the energy input into the magnetosphere is considerably larger for large ICME-driven events, the difference being that the forcing can be sustained over longer intervals for some CIRs than ICMEs.

At solar minimum, when ICMEs are less frequent, CIRs play a dominant role as a source of geomagnetic disturbances [*Gonzalez et al*., 1999; *Tsurutani et al*., 1995; 2006; *Xu et al*., 2009; *Cramer et al*., 2013]. *Richardson et al.* [2001] studied the drivers of the largest storms (defined using the *Kp* index) and found that 97% were driven by ICMEs, both at sunspot maximum and sunspot minimum. Similarly, by looking at intense storms (defined by $Dst \leq -100$ nT) over the interval 1998–2008, *Xu et al.* [2009] found that 74% were driven by ICMEs with magnetic clouds and a further 7% by ICMEs without an MC. Storms are the extreme end of a distribution of disturbances, and because the distribution can change shape, their occurrence at a given disturbance level can vary in a different way to the mean value of the distribution. *Richardson et al.* [2002] used the range *aa* geomagnetic index (which, like *Kp* and the a_m index, responds primarily to substorm expansion phases) over three solar cycles to study the contributions of the various types of solar wind and transients to average geomagnetic activity. They showed that high-speed streams and CIRs were the largest contributor to the average *aa* levels at solar minimum, accounting for about 67%, whereas at solar maximum, structures associated with transients (ICMEs and MCs) made the largest contribution (≈50%).

2.3. Effect of Timescale

Timescale is an important factor when considering geoeffectiveness of the solar wind and embedded IMF. *Finch and Lockwood* [2007] studied the performance of various solar wind "coupling functions" (combinations of solar wind and IMF parameters designed to quantify consequent terrestrial disturbance levels) in predicting various geomagnetic indices for averaging timescales *T* which they varied between 1 day and 1 year. The optimum coupling function was shown to vary with the timescale considered. For example, because the magnetosphere responds to the southward component of the IMF in the GSM frame, functions of the form $B\sin^4(\theta/2)$, where B is the IMF magnitude and $\theta = \tan^{-1}\{B_Y(\mathrm{GSM})/B_Z(\mathrm{GSM})\}$ is the IMF "clock angle" in the GSM *Z*-*Y* plane, are very successful on short timescales ($B\sin^4(\theta/2)$ is roughly equivalent to B_S(GSM) but has the advantage of being continuous in slope). However, for longer averaging timescales the orientation factor $\sin^4(\theta/2)$ averages to an almost constant value [*Stamper et al*., 1999; *Lockwood*, 2013] and B becomes as successful as $B\sin^4(\theta/2)$ (and, indeed, generally out-performs it because the main effect of the $\sin^4(\theta/2)$ factor is to introduce additional observational noise). As pointed out by *Lockwood* [2013], this is a key factor that allows the IMF, open solar flux, and solar wind speed to be reconstructed from annual means of historic geomagnetic data [*Lockwood et al*., 1999; *Lockwood et al*., 2014].

The timescale effect, and hence the optimum coupling function for that timescale, depends on the activity index employed: For example, *Huttunen et al.* [2002] noted that all storms influence both the *Dst* and *Kp* geomagnetic indices, but the rank order of the severity of those storms is strongly dependent on whether *Kp* or *Dst* is considered. Hence, there is no such thing as an all-encompassing interplanetary coupling function which can predict all aspects of disturbance in the magnetosphere-ionosphere-thermosphere system.

Consider the *AU* index: This is designed to detect the eastward electroject in the afternoon sector auroral oval, which is the current associated with dayside ionospheric convection driven by low-latitude magnetopause reconnection. It responds rapidly (within a few minutes) and directly to southward IMF at the dayside magnetopause [*Nishida*, 1968; *Etemadi et al*., 1988; *Todd et al*., 1988] and so is predicted by B_S(GSM) or $B\sin^4(\theta/2)$, averaged over timescales T of just a few minutes. On the other hand, the *AE* and *AL* indices detect the auroral electroject of the nightside substorm current wedge and so respond to the integrated effect of B_S(GSM) or $B\sin^4(\theta/2)$, over the substorm growth phase which typically lasts for between 20 and 60 min [*Baker et al*., 1983]. Hence, half-hourly or hourly averages are more appropriate when predicting these indices. The mid-latitude "range" geomagnetic indices such as *aa*, *Ap*, *Kp*, and a_m respond strongly to the number and strength of substorm expansion phases in the 3 h interval that they are compiled over (see review by *Lockwood* [2013]), and so 3-hourly means of the IMF data are more appropriate. The transpolar voltage Φ_{PC} is understood to be a combination of the effect of both the dayside (magnetopause) and nightside (tail current sheet) reconnection voltages, Φ_D and Φ_N, respectively [*Lockwood et al*., 1990; *Cowley and Lockwood*, 1992], which differ from each other on timescales shorter than the substorm cycle length, other than during very quiet conditions and perhaps during some steady convection events [*Lockwood et al*., 2009]: For a circular polar cap $\Phi_{PC} = (\Phi_D + \Phi_N)/2$. Hence, transpolar voltage will correlate best with B_S(GSM), or perhaps the dawn-to-dusk interplanetary magnetic field, E_Y(GSM) $= -V_X B_S$(GSM), for timescales T that average out the variations such that $<\Phi_D>_T = <\Phi_N>_T = <\Phi_{PC}>_T$, in other words that T is great enough for steady state to apply. This requires averaging over several substorm cycles (in general, over any one substorm cycle not all the open flux built up in the growth phase is destroyed in the subsequent expansion and recovery phases): hence, averaging over T of a day or more is entirely appropriate. We note here that *Thomsen* [2004] explains the strong relationship between convection and the *Kp* index in terms of the sensitivity of this index to the equatorward part of the auroral electrojet and how that moves equatorward with the inward motion of the inner edge of the plasma sheet when convection is enhanced. This is consistent with the idea used here that *Kp* responds mainly to substorms, given that the auroral electrojet is dominated by substorm expansion phases and convection can be viewed as being predominantly the integrated effect of substorm cycles [*Lockwood et al*., 1990; *Cowley and Lockwood*, 1992; *Lockwood et al*., 2009].

In many studies, the *Dst* index has been used to evaluate geoeffectiveness [e.g., *Burton et al*., 1975; *Echer and Gonzalez*, 2004; *Alves et al*., 2006; *Denton et al*., 2006; *Lavraud et al*., 2006]. The *Dst* index is measured by a ring of four low-latitude geomagnetic stations and was designed to be an index of the ring current (note, however, that it is inevitably also influenced by other currents in the magnetosphere-ionosphere system). *Dst* is the index generally used to define storms rather than substorms. *Temerin and Li* [2002] model *Dst* with components that are driven by IMF B_S(GSM), but with decay time constants, for a typical *Dst* of 20 nT, 11.4 h, and 5.1 days. In fact, *Cliver et al.* [2000] show that the behavior of the time derivative of *Dst* is somewhat similar to the range indices like a_m (for d*Dst*/d*t*, the t-o-y/t-o-d pattern that is midway between an axial and an equinoctial form). This implies that *Dst* behaves, to some extent, like the time integral of substorm behavior. However, as discussed further in section 3.1, the storm-substorm relationship is more complex than this. *Dst* currents are also enhanced by particle injections that are not directly related to substorms, but which occur during steady convection events, as well as by substorm-associated injections [*Reeves and Henderson*, 2001; *Lui et al*., 2001; *Reeves et al*., 2003]. This is discussed further in section 3.1: the point that we wish to highlight here is that either mechanism (a string of substorms or a steady convection event) will enhance *Dst* most if strong southward IMF persists over a prolonged period. Indeed, *Echer et al.* [2008] show that the interplanetary parameter that best predicts "superstorms" in solar cycle 23 (defined as $Dst \leq -250$ nT) is the integral of the dawn-to-dusk interplanetary electric field E_Y(GSM) over the duration of the storm. Given that these events last several days, this argues that the most appropriate averaging timescale T for the largest possible events will be of order 2 or 3 days.

2.4. Smaller-Scale Solar Wind Structure

In addition to the large-scale heliospheric structures such as CIRs, ICMEs, and sector boundaries, in situ spacecraft observations show fluctuations in the IMF due to waves, shocks, turbulence, weak stream-stream interactions, and small MCs [*Matthaeus et al*., 1986; *Horbury et al*., 2001; *Bruno et al*., 2001; *Bruno and Carbone*, 2013]. In addition there may be "fossil" features formed by, for example, stream-stream interactions closer to the Sun that persist after the causal interaction has decayed away [*Owens et al*., 2011].

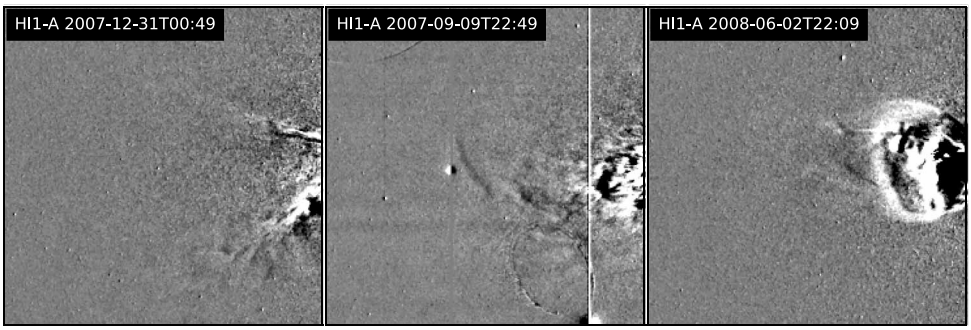

Figure 4. Difference images from the HI-1 instrument on the STEREO-A satellite with the Sun just to the right of each image. White/black areas are where received intensity of Thompson scattered light is increasing/decreasing: (a) shows a period of quiet solar wind between transients; (b) shows a Corotating interaction region, CIR (just on the sunward side of the planet); and (c) shows an erupting coronal mass ejection, CME. The dates and times of the observations are given in the top left of each frame.

New information on solar wind structure has recently been obtained from heliospheric imaging techniques. The Heliospheric Imagers (HI) on the STEREO spacecraft have been used to detect and monitor the propagation of both CIRs [*Rouillard et al*., 2008] and ICMEs [*Davis et al*., 2009]. The HI cameras detect sunlight that has been Thompson scattered by electrons in the heliosphere and by dust. Because the latter (the "*F* corona") varies relatively slowly, it is removed by taking the difference in intensity at each point in successive images, which highlights moving plasma density structures. Figure 4 shows three examples of such "difference images" recorded by the HI-1A instrument on STEREO-A, in which increasing/decreasing solar wind plasma density appears as lighter/darker regions, respectively, and so a traveling transient enhancement appears as a lighter region followed by a darker one. The Sun is just to the right of each frame. Figure 4a reveals variety of structures with a range of spatial scales in the quiet solar wind. Figure 4b shows an example of a CIR, and Figure 4c shows an example of an ICME. Movies of these difference images are particularly effective in revealing the wealth of density structures in the solar wind. *King and Papitashvili* [2005] show that the structure in the IMF, detected in situ using pairs of interplanetary craft, has tended to be smaller scale than the structure in the solar wind that HI typically observes. Using HI images and in situ data, *Kilpua et al.* [2009] and *Yu et al.* [2014] have surveyed small transient (ST) events which would pass over Earth in between a few tens of minutes and several hours. Some are entrained in CIRs [*Rouillard et al*., 2009, 2010a, 2010b], but they are also seen in the "quiet" solar wind away from such structures. In these ST events there is microscale structure in the field and a smooth rotation giving more geoeffective intervals of southward IMF in some cases. Of order 50% are Alfvénic events [*Yu et al*., 2014], but the remainder were mainly found convecting in the slow solar wind but not expanding and are thought to originate from the plasma blobs which *Sheeley et al.* [1999] discovered to emanate from streamer cusps. *Sheeley et al.* [2009] have demonstrated that these blobs are, at least initially, rising arches that appear to be flux ropes.

3. Analysis of Near-Earth Interplanetary Data From 1996–2015

In this paper we use the Omni-2 hourly interplanetary data set for the 20 year interval between 1 January 1996 and 1 January 2016 [*King and Papitashvili*, 1994]. This interval was chosen because the data are almost continuous, coming mainly from the ACE and WIND spacecraft, close to the L1 Lagrange point. All data have been lagged by the predicted propagation delay from the satellite to the dayside magnetopause. Note that the sunspot minimum between cycles 22 and 23 occurred in 1996, and so the 20 years studied here covers all of cycle 23 and most of cycle 24: the last part of the full Hale solar polarity cycle (≈22 year duration) will be the late declining phase of cycle 24 over the next 2–4 years. The Cane and Richardson list of ICMEs has been updated to the end of the period and so provides us with list of the major ICMEs that impacted near-Earth space at L1 for the whole of this interval. Note that to be a valid average of interplanetary observations, we here require at least 75% data availability in the hour: over 1996–2015 this yields 174,990 hourly means of data.

As in other studies discussed in the introduction, we here use the *Dst* index to identify storms, defined as being when $Dst < Dst_o$. The severity of the storms considered is varied by employing various values of the

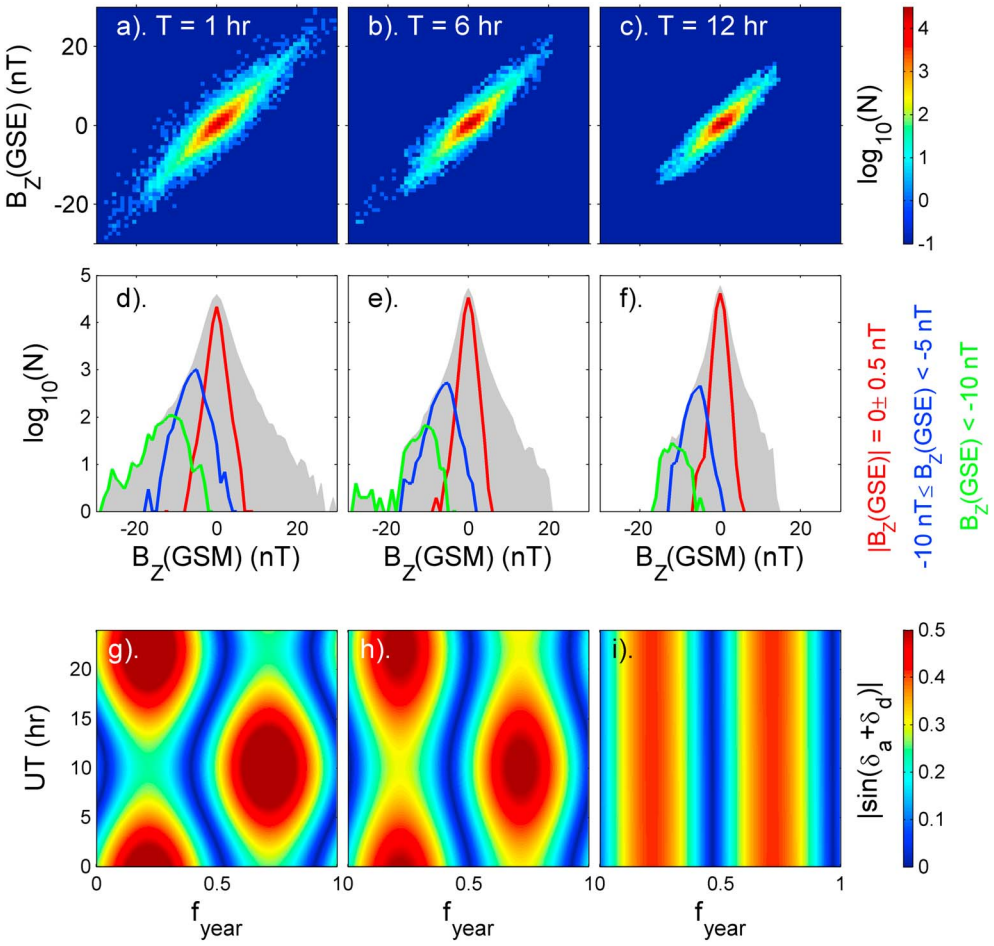

Figure 5. (a–c) The numbers of IMF observations, N, in 1 nT bins of B_Z(GSM) (horizontal axis) and B_Z(GSE) (vertical axis): Bins are colored according to $\log_{10}(N)$ using the color scale shown. (d–f) Distributions of $\log_{10}(N)$ with B_Z(GSM): The grey shaded area shows the distribution for all B_Z(GSE); the red line is for in-ecliptic field ($-0.5\,\text{nT} \le B_Z(\text{GSE}) < +0.5\,\text{nT}$); the blue line for $-10\,\text{nT} < B_Z(\text{GSE}) \le -5\,\text{nT}$; and the green line for strongly southward out-of-ecliptic field, $B_Z(\text{GSE}) \le -10\,\text{nT}$. (g–i) Time-of-day/time-of-year plots of $|\sin(\delta_a + \delta_d)|$, where $(\delta_a + \delta_d)$ is the rotation angle around the X axis between the GSE and GSM reference frames. Data are for 1 January 1996–31 December 1915 and are for averaging timescales of $T = 1$ h for Figures 5a, 5d, and 5g; $T = 6$ h for Figures 5b, 5e, and 5h; and $T = 12$ h for Figures 5c, 5f, and 5i.

threshold value, Dst_o. The Dst index is available from 1957. Unless otherwise stated, data for 1996–2015 are used to match the IMF data coverage.

3.1. The Relative Effects of Geometric Factors and Out-of-Ecliptic Field

From the discussion in section 2, we can divide the origins of geoeffective IMF into two classes. The first is field that lies in, or near-parallel-to, the solar equatorial plane and hence to the ecliptic plane ($B_Z(\text{GSE}) \approx 0$) but acquires a southward component in the GSM frame ($B_Z(\text{GSM}) < 0$) because of a favorable orientation of the geomagnetic dipole axis under the effects of Earth's orbital motion and rotation. The second cause is field that has a large southward out-of-ecliptic field in the GSE frame ($B_Z(\text{GSE}) < 0$). These two effects, in general, combine and at any one time the dipole tilt effects can act to either increase or decrease the effects of southward out-of-ecliptic field. To analyze the overall importance of these two factors, Figure 5 (a–c) presents plots of the number of occurrences of samples, N, (colored according to a logarithmic scale and for all data from 1996 to 2015) in 1 nT bins of B_Z(GSM) (along the horizontal axis) and of B_Z(GSE) (along the vertical axis). Because of the importance of averaging timescale discussed in section 2.3, plots are made for $T = 1$ h, shown in Figure 5a, and 1 h data converted to running (boxcar) means for averaging intervals of (Figure 5b) $T = 6$ h, and (Figure 5c) $T = 12$ h. In all three panels, the points cluster along the diagonal (for which $< B_Z(\text{GSM}) >_T = < B_Z(\text{GSE}) >_T$). Hence, the orientation factor introduces no bias but does introduce

scatter. Moving to longer averaging timescales reduces this scatter but also reduces the range of values detected. For all three T values, the strongest southward IMF in the GSM frame always occurs when there is also strong southward out-of-ecliptic field component in the GSE frame. The R-M effect causes the scatter in the plot and for Figure 5a this includes the effect of both the t-o-y and t-o-d variations, whereas in Figure 5c the scatter is almost entirely due to the t-o-y variation alone as the diurnal variation has been almost completely averaged out.

Figures 5d–5f shows distributions of $\log_{10}(N)$ as a function of B_Z(GSM) for the same three averaging timescales T. In each of these plots, the grey shaded area is the distribution of B_Z(GSM) values for all B_Z(GSE), the red line for near-in-ecliptic field (B_Z(GSE) between − 0.5 nT and +0.5 nT), the blue line for strong southward out-of-ecliptic field (B_Z(GSE) between − 5 nT and − 10 nT), and the green line for exceptionally strong southward out-of-ecliptic field (B_Z(GSE) < -10 nT). The three plots show that distributions are increasingly narrow for increasing T but that, in all three cases, the most geoeffective fields (the most negative B_Z(GSM) values) are always associated with strong out-of-ecliptic field in the GSE frame.

Figures 5g–5i show the t-o-d/t-o-y plots of the sine of rotation angle around the X axis between the GSE and GSM reference frames. Each panel shows $|<\sin(\delta_a+\delta_d)>_T|$ color contoured as a function of fraction of the year, f_{year} (horizontal axis) and the UT (vertical axis), where δ_a and δ_d are the annual and diurnal components caused by the tilt of Earth's rotation axis and the offset of rotational and geomagnetic axes, respectively (as defined in Figure 1). The angle $(\delta_a+\delta_d)$ is the basis of the R-M effect, and Figure 5g shows the classic R-M pattern, as also shown in Figure 2a. Comparison in Figures 5g and 5h shows that averaging has little effect up to timescales of $T=6$ h and the R-M pattern is still clearly seen (the peaks are slight reduced magnitude and are slightly elongated in the vertical direction). However for $T=12$ h (Figure 5i) the diurnal variation is averaged out and the pattern has become completely "axial" in form, like Figure 2c. Thus, for terrestrial disturbances that involve forcing over 12 h or more the pattern for the R-M effect will give an axial t-o-d/t-o-y response pattern rather than the well-known R-M form that is seen for T less than about 6 h. *O'Brien and McPherron* [2002] show that large particle injections into the ring current display an axial dependence, which contrasts with the magnetic indices that respond strongly to substorms, and which reveal an equinoctial pattern (such as a_m in Figure 2e) [*Cliver et al*., 2000; *Finch et al*., 2008]. This discrepancy does, therefore, not appear to fit with the old view of large injections being a substorm phenomenon. However, *Reeves and Henderson* [2001] and *Lui et al.* [2001] have provided an explanation in which injections are driven by enhanced convection events as well as by substorms and that it is the former that has the more lasting effect in enhancing the ring current. This being the case, we would expect sustained forcing to be more relevant and the t-o-d/t-o-y pattern for large T, which Figure 4i shows axial in form, to be relevant to both particle injections and *Dst*. Although injections do show an axial t-o-y/t-o-d pattern [*O'Brien and McPherron*, 2002], the corresponding pattern for *Dst* is close to, but not quite, axial [*Cliver et al*., 2000]: It shows the axial annual structure of Figure 2c but also with a UT variation in the equinoctial peaks with a minimum index response around 12 UT. *Takalo and Mursula* [2001] have demonstrated that this UT variation arises from the longitudinal distribution of the equatorial *Dst* stations, implying that the underlying t-o-y/t-o-d variation in *Dst* is indeed axial in form. Figure 2f shows t-o-y/t-o-d pattern for *Dst* after it has been multiplied by the factor $-k$(UT) modeled by *Takalo and Mursula* [2001] that allows for the fact that the four *Dst* stations are not equally spaced in longitude. With this correction, the *Dst* pattern is clearly axial in form. However, close inspection shows that the maxima in Figure 2f are slightly after those in Figure 2c, being more centered on the equinoxes than the dates of peak $|\sin(\Lambda_E)|$ (the former being 20 days earlier than the latter). As noted by *Russell and McPherron* [1973], this indicates that this axial effect is more likely to be associated with the annual part of the dipole tilt effects than the annual variation in the heliographic latitude of Earth, Λ_E. Figure 5i demonstrates how this axial pattern would be consistent with the R-M effect because of the long timescales of the *Dst* index response, as discussed in section 2.3.

Figure 6 presents a detailed analysis of the relative roles of the out-of-ecliptic field and the geometric (R-M) effect in driving major storms, as detected in the *Dst* index. Figures 6a, 6d, and 6g are the same as Figure 5a but limited to times when geomagnetic activity subsequently revealed a magnetic storm (identified by when the *Dst* index fell below a threshold value, Dst_o, within the next 12 h). All times when hourly means of *Dst* fell below the threshold value were identified, giving the results shown in Figures 6a–6i for Dst_o of − 100 nT, −150 nT, and − 200 nT, respectively. For each such hour, the most geoeffective IMF (the largest $B\sin^4(\theta/2)$ value in hourly means) in the prior 12 h was identified (including the hour in question, after the

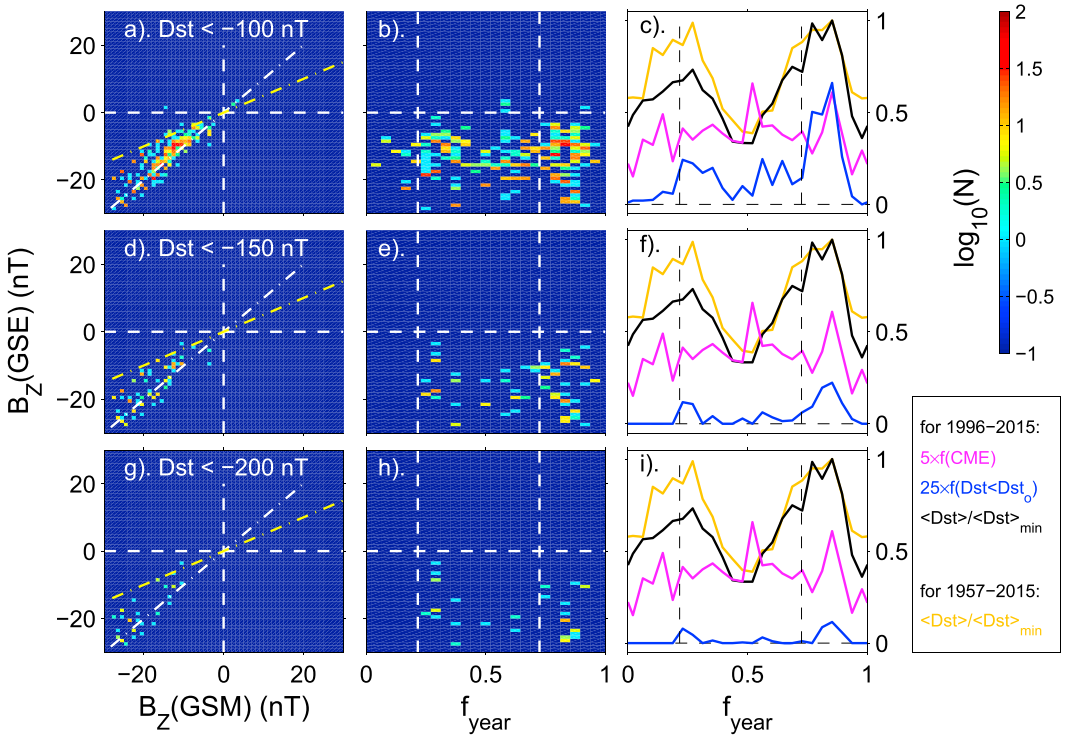

Figure 6. Analysis of contribution to storms, as defined by the *Dst* index. Figures 6a, 6d, and 6g show the number *N* (on the logarithmic scale given) of hourly means ($T = 1$ h) in 1 nT bins of $< B_z(\mathrm{GSE}) >_T$ (vertical axis) and $< B_z(\mathrm{GSM}) >_T$ (horizontal axis) for the 1996–2015 IMF data set. Values are shown for the most negative $< B_z(\mathrm{GSM}) >_T$ in the 12 h prior to each observation of $Dst < Dst_o$, where the *Dst* threshold, Dst_o, is (a–c) −100 nT, (d–f) −150 nT, and (g–i) −200 nT. The horizontal and vertical white dashed lines in Figure 6a, 6d, and 6g are for $B_z(\mathrm{GSE}) = 0$ and $B_z(\mathrm{GSM}) = 0$, respectively, the diagonal white dash-dotted line is for $B_z(\mathrm{GSE}) = B_z(\mathrm{GSM})$ and the yellow dash-dotted line is for $B_z(\mathrm{GSM}) = 2 \times B_z(\mathrm{GSE})$. Figures 6b, 6e, and 6h show the same for 1 nT bins of $B_z(\mathrm{GSE})$ along the vertical axis and (1/24) year bins of the time-of-year (f_{year}, which varies from zero on 1 January to unity on 31 December) along the horizontal axis. The horizontal dashed line is for $B_z(\mathrm{GSE}) = 0$, and the two vertical dashed lines mark the March and September equinoxes. (c, f, and i) display some mean annual variations. The blue lines show $25 \times f(Dst < Dst_o)$ where $f(Dst < Dst_o)$ is the fraction of hours of $Dst < Dst_o$, for the same thresholds, Dst_o, as the other two panels in each row. Figures 6c, 6f, and 6i also show three other variations in (1/24) year bins of f_{year}: (mauve line) $5 \times f(\mathrm{CME})$, where $f(\mathrm{CME})$ is the fraction of time when near-Earth space is perturbed by an identified ICME; (black line) the mean *Dst* normalized to its maximum amplitude (minimum *Dst*) for data from 1996 to 2015, $<Dst>/<Dst>_{min}$; and (orange line) $<Dst>/<Dst>_{min}$ for the full *Dst* data set, covering 1957–2015.

satellite-to-magnetopause propagation delay had been allowed for). The interval of 12 h was chosen from the analysis of timescales discussed in section 3.3: in fact, a range of values between 0 and 24 h was tried and the plots were not significantly different from those shown in Figure 6. The corresponding B_z(GSE) value and the fraction of the year, f_{year}, at that time were then defined. Figures 6a, 6d, and 6g show the numbers *N* of these values of peak geoeffective field estimates ahead of each storm (on the logarithmic scale shown) as a function of B_z(GSM) and B_z(GSE). Points conforming to the idealized R-M effect (with $B_z(\mathrm{GSE}) = 0$ but $B_z(\mathrm{GSM}) < 0$ due to a favorable dipole tilt angle) would lie along the horizontal dashed line. There is just one example that fits this scenario for $Dst_o = -100$ nT and none for $Dst_o = -150$ nT nor $Dst_o = -200$ nT. Almost all points lie within the $B_z(\mathrm{GSE}) < 0$ and $B_z(\mathrm{GSM}) < 0$ quadrant and many lie on the diagonal white dash-dotted line where $B_z(\mathrm{GSE}) = B_z(\mathrm{GSM})$ (i.e., examples of storms where the geometric R-M effect has had no influence). There is a small minority of points to the right of this diagonal, for which the R-M effect has actually reduced the geoeffectiveness of the southward out-of-ecliptic field and yet a storm, at the required Dst_o level, still occurred. The great majority of cases are to the left of the diagonal, meaning that the R-M effect has combined with the out-of-ecliptic field to enhance the disturbance. The yellow dash-dotted line is where $B_z(\mathrm{GSM}) = 2 \times B_z(\mathrm{GSE})$. To the left of this line, the geometric factor has contributed more than the out-of-ecliptic field. Such cases are rare; less than 10 in number for $Dst_o = -100$ nT, and there is just one case for $Dst_o = -150$ nT and for $Dst_o = -200$ nT. *Temerin and Li* [2002], like *Russell and McPherron* [1973] and *Crooker et al.* [1992],

invoke the R-M effect as an important factor in driving storms. Here we find that in the vast majority of cases, the storm is associated with a dominant effect of out-of-ecliptic field with a minor contribution from the R-M geometric effect (between the white and yellow dash-dotted lines) and there are even a number of cases in which the R-M effect worked to reduce the geoeffective field but not by so much that it prevented a storm.

3.2. The Semiannual Variation

Russell and McPherron [1973] argued that the R-M effect was the cause of the enhanced occurrence of large geomagnetic storms at the equinoxes. A key test of the idea that the R-M effect is central to any semiannual variation was made by *Zhao and Zong* [2012]. These authors showed that which of the two equinoxes was favored in generating geomagnetic activity depended on the polarity of the IMF B_Y(GSE) component. This is a unique prediction of the R-M effect, as discussed section 2. On the other hand, Figures 5 and 6 show that although the R-M effect is a factor in solar wind magnetosphere coupling, large storms almost always follow strong southward, out-of-ecliptic field in the GSE frame. This section discusses these apparently contradictory findings.

Figures 6b, 6e, and 6f show the occurrence of the lowest B_z(GSE) hourly values as a function f_{year} for all cases when a storm that exceeded the Dst_o threshold followed in the subsequent 12 h. All data are for (1/24) f_{year} bins. The tendency for storms to occur around the equinoxes can be seen. Figure 6b, for $Dst_o = -100$ nT, shows that storms for smaller $|B_Z(GSE)|$ are more clustered around the equinoxes ,whereas for more southward B_Z(GSE), they are more evenly distributed through the year. The same feature can be seen for $Dst_o = -150$ nT (Figure 6e) and $Dst_o = -200$ nT (Figure 6f), even though the number of storms is much smaller.

The blue line in each plot in the right-hand column of Figure 6 shows the fraction of hours that *Dst* is less than the Dst_o value, $f(Dst < Dst_o)$ for the Dst_o of that row and compares it to three other annual variations. Note that each $f(Dst < Dst_o)$ variation has been multiplied by 25 to put it on the common scale between 0 and 1 given on the right-hand side of each panel. The black lines in each of these plots show the annual variation of the average value of *Dst*, normalized by dividing by its largest negative value $<Dst>/<Dst>_{min}$ for the 1996–2015 interval (note that both $<Dst>$ and $<Dst>_{min}$ are negative so $<Dst>/<Dst>_{min}$ is positive). For these data, the semiannual variation is clear but the March equinox peak is considerably smaller than the September one. This is not a general feature: the orange line again shows $<Dst>/<Dst>_{min}$, but for the full *Dst* data set (1957–2015). For this longer data set, the March and September peaks are comparable. The lower peak for March in the shorter data set may be due to biases introduced by the missing part of the Hale cycle in the 1996–2015 data set (introducing a bias into B_z(GSM) via the combined R-C/R-M effect) and/or the fact that solar cycle 24 is much less active than cycle 23. For all three Dst_o levels, the annual variation in the occurrence of storms with $Dst < Dst_o$ in 1996–2015 mirrors the annual variation in mean *Dst* to some extent.

Lastly, the mauve lines in Figures 6c, 6f, and 6i show the fraction of time that the near-Earth satellite is within a defined ICME (see section 3.4), *f*(CME) (here multiplied by 5 for the same scale). Although there is considerable bin-to-bin variability, *f*(CME) does not show any clear semiannual variation. This is consistent with surveys of the heliographic latitudinal distribution of CME occurrence. For example, *Yashiro et al.* [2004] surveyed 7000 CME events between 1996 and 2002. For 1997 (near sunspot minimum), 80% of CMEs were centered on a heliographic latitude of 17°S and 21°N—a distribution that is narrow enough for the variation of Earth between 7°S and 7°N could decrease the ICME occurrence at Earth at the equinoxes. However, because the average latitudinal width of each CME at this time was 47°, the effect is negligibly small. By 2006 (near sunspot maximum) 80% of CMEs were between 61°S and 65°N in a flat-topped distribution, so no annual variation in CME occurrence is expected to result from the annual variation in Earth's heliographic latitude.

Figure 7 investigates the annual variations further. Figure 7a shows the mean values of $<Dst>$ and the number of hours when *Dst* is lower than a threshold value of $Dst_o = -200$ nT. In both cases the red/black line is for hours when the mean IMF $<B_Y(GSE)>_T$ over the prior $T = 12$ h was positive/negative. The $<Dst>$ values are all negative and reveal unambiguously the R-M effect with larger disturbances near the March/September equinoxes when the prior IMF B_Y(GSE) has been predominantly negative/positive, respectively. As noted by *Zhao and Zong* [2012], this is a unique signature of the R-M effect. The number of storm hours with $Dst_o < Dst_o$ (for which values are always positive) does show this effect, but it is much less pronounced. The effect is more clearly present for $Dst_o = -100$ nT (not shown) but becomes increasingly weaker for larger

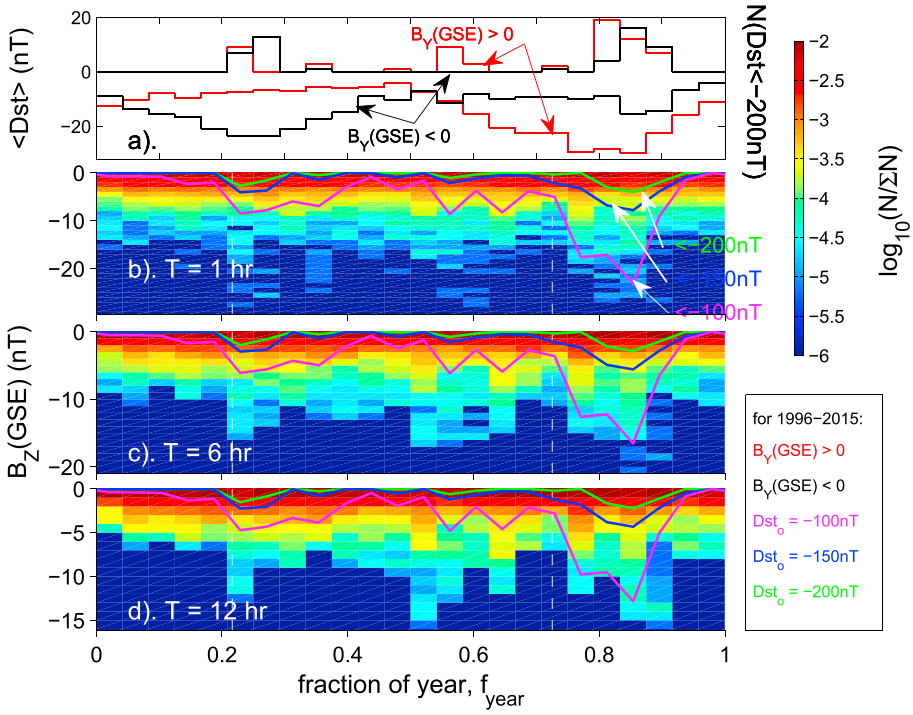

Figure 7. (a) The mean *Dst* and the number of hours of *Dst* below the threshold Dst_o of −200 nT, $N(Dst < -200\,nT)$ as a function of t-o-y (f_{year}): red/black lines are for when the mean IMF B_Y(GSE) in the previous 12 h was positive/negative, respectively. Negative values are $< Dst >$, positive values are $N(Dst < -200\,nT)$. (b, c, and d) The occurrence of southward IMF B_z(GSE) as a function of time-of-year, f_{year}, for averaging timescale T of (1) 1 h, (2) 6 h, and (3) 12 h. The number of samples, N, in 1 nT bins of B_z(GSE) and (1/24) bins of f_{year} is shown, normalized to the total number for that f_{year} bin, ΣN. Note that each pixel is colored on a logarithmic scale of $N/\Sigma N$. By using a maximum of zero on each B_z(GSE) axis, the plots show only the results for southward IMF. Note also that different B_z(GSE) scales are used for the three panels because the distributions are narrower for larger T. Each panel also shows the number of hours, times a negative constant ($c < 0$), of $Dst < Dst_o$ for thresholds of (mauve line) $Dst_o = -100$ nT, (blue line) $Dst_o = -150$ nT, and (green line) $Dst_o = -200$ nT. The value of c is different in the three panels and c is negative to make visual comparison with the B_z(GSE) occurrence easier. Vertical dashed white lines mark the equinoxes.

disturbances, such as for the $Dst_o = -200$ nT case that is shown. Although there is still an effect of the prior IMF B_Y(GSE), it is much less pronounced for the large storms than for the mean values.

The colored pixels in the other panels of Figure 7 show N, the number of negative B_z(GSE) samples in 1 nT bin of B_z(GSE) and (1/24) bins of the time-of-year fraction, f_{year}: Figure 7b is for averaging timescale $T = 1$ h, Figure 7c is for $T = 6$ h, and Figure 7d is for $T = 12$ h. On each panel are also plotted the occurrences of large *Dst* disturbances (times a negative constant, c), quantified by the number of hours giving $Dst < Dst_o$ for thresholds of $Dst_o = -100$ nT (mauve line), $Dst_o = -150$ nT (blue line) and $Dst_o = -200$ nT (green line). For all three thresholds there are peaks in the occurrence of storm-level *Dst* values are quite close to the equinoxes (marked by the vertical dashed lines): The peaks for $f_{year} < 0.5$ are all close to the March equinox but the peaks for $f_{year} > 0.5$ are all notably after the September equinox. The peaks in these occurrences can be seen to be accompanied by an increase in the number of larger negative B_z(GSE) in the 1 h means (Figure 7 b) but not all such occurrences cause large negative *Dst*. A relationship is much clearer for longer averaging timescales of $T = 6$ h. (Figure 7c) and most clear for $T = 12$ h (Figure 7d).

The mauve curves in Figures 6a, 6d, and 6g show that there is a peak in the occurrence of ICMEs at Earth, f(CME), between the September equinox and the December solstice that coincides with the peak in the occurrence of large-storm hours, $f(Dst < -200\,nT)$. At this peak there is little or no R-M effect for the largest storms, with $< Bz(GSE) >_T \approx < Bz(GSM) >_T$ (for $T = 12$ h) and the storms occurring roughly equally for the two polarities of $< B_Y(GSE) >_T$. However, there is no such peak in f(CME) at the March equinox and yet there is a peak, albeit a smaller one, in $f(Dst < -200\,nT)$ and enhanced, long-lived southward field seen in $< B_z(GSE) >_T$. Again, at this peak there is little R-M effect for the strongest storms ($< Bz(GSE) >_T \approx < Bz(GSM) >_T$

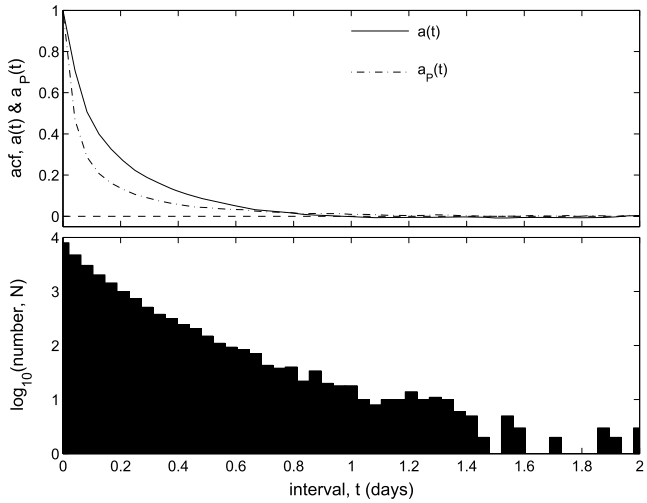

Figure 8. Effects of timescale on the IMF B_Z(GSE) component. (top) The solid line is the autocorrelation function (acf) $a(t)$ of B_Z(GSE) and the dash-dotted line is the acf $a_P(t)$ of the polarity of B_Z(GSE), P_Z(GSE), as a function of lag, t. (bottom) The logarithm of the number of intervals, N, of constant southward polarity P_Z(GSE) < 0 lasting between t and $t + dt$ for dt of 1 h, as a function of t.

and no preference for either polarity of $< B_Y$(GSE) $) > T$ for the f_{year} bin around March equinox (although there is for the subsequent f_{year} bin). The strongest peak of all in f(CME) is found just after $f_{year} = 0.5$ and is accompanied by enhanced, long-lived southward field but only a very weak response in $f(Dst < -200$ nT).

Thus, the cause of the annual variation in the largest storms shown in Figures 6 and 7 is complex. The largest feature in the annual variation for the last 20 years appears to be caused by the effect of the stochastic nature of ICME occurrence at Earth and hence of their associated large, persistent, out-of-ecliptic southward field, hitting Earth's magnetosphere. Because we are dealing with a very small number of $Dst < -200$ nT events, this stochastic nature is apparent, even in this 20 year survey. Chance is also the most likely explanation of why ICME events and storms around $f_{year} = 0$ have been much rarer than around $f_{year} = 0.5$; however, the events that occurred around $f_{year} = 0.5$ caused notable fewer storm hours than the events that followed the March and September equinoxes.

Figures 6 and 7 help us understand the relative roles of out-of-ecliptic field and the R-M effect in generating storms. Some storms are caused purely by out-of-ecliptic southward IMF, and we infer that these can occur at any phase of the year. (However, the release times of CMEs introduces a random sampling effect when we look at the very small number of very large events) Other storms are also predominantly caused by out-of-ecliptic southward IMF but have been enhanced by a favorable R-M effect. The larger the contribution of the R-M effect, the more likely the storm is to be around the equinox. The larger the storm, the smaller the R-M contribution.

There is one other possibility we should address. There is no doubt that the R-M effect is clearly present in average *Dst* values, and so it is possible that more disturbed average conditions, ahead of the arrival of the event driver, could precondition the magnetosphere, making the storm magnitude larger for a given magnitude of geoeffective field within the event driver. Note that this effect, if present, would be the opposite of the preconditioning proposed by *Lavraud et al.* [2006] and *Borovsky and Denton* [2006] which is due to a prior period of northward IMF (as discussed in section 2.2). This would allow the R-M effect to impose an annual variation even if it was not itself a significant contributor to the geoeffective field of the event driver. However, we could find no statistical evidence for any such effect in the limited number of storm events available in the data set.

3.3. Timescale of Out-of-Ecliptic Field Variations

In this paper, we investigate the effects of both persistence and magnitude of out-of-ecliptic IMF. The solid and dash-dotted lines in Figure 8 (top) show the overall autocorrelation functions ("acfs") of hourly means of, respectively, B_z(GSE) and P_z(GSE), where P_z(GSE) is the polarity of B_z(GSE) (defined by P_z(GSE) = +1 for B_z(GSE) $\geq$ 0.1 nT, P_z(GSE) = −1 for B_z(GSE) ≤ -0.1 nT and P_z(GSE) = 0 for 0.1 nT $> B_z$(GSE) > -0.1 nT). These acfs are, respectively, termed $a(t)$ and $a_P(t)$ and are derived from the 1996–2016 data set. Both acfs are close to zero at a lag t of 1 day and much of the variability causing this is in the polarity of B_z(GSE) as $a_P(t)$ is a narrower acf than $a(t)$. Figure 8 (bottom) shows the number of intervals, N, for which the IMF maintains a southward polarity (in the GSE frame) for between t and $t + dt$ (for dt = 1 h) as function of t. Note that $\log_{10}(N)$ is plotted. The vast majority of intervals of southward IMF are under a day in duration, giving the acfs shown in the top interval.

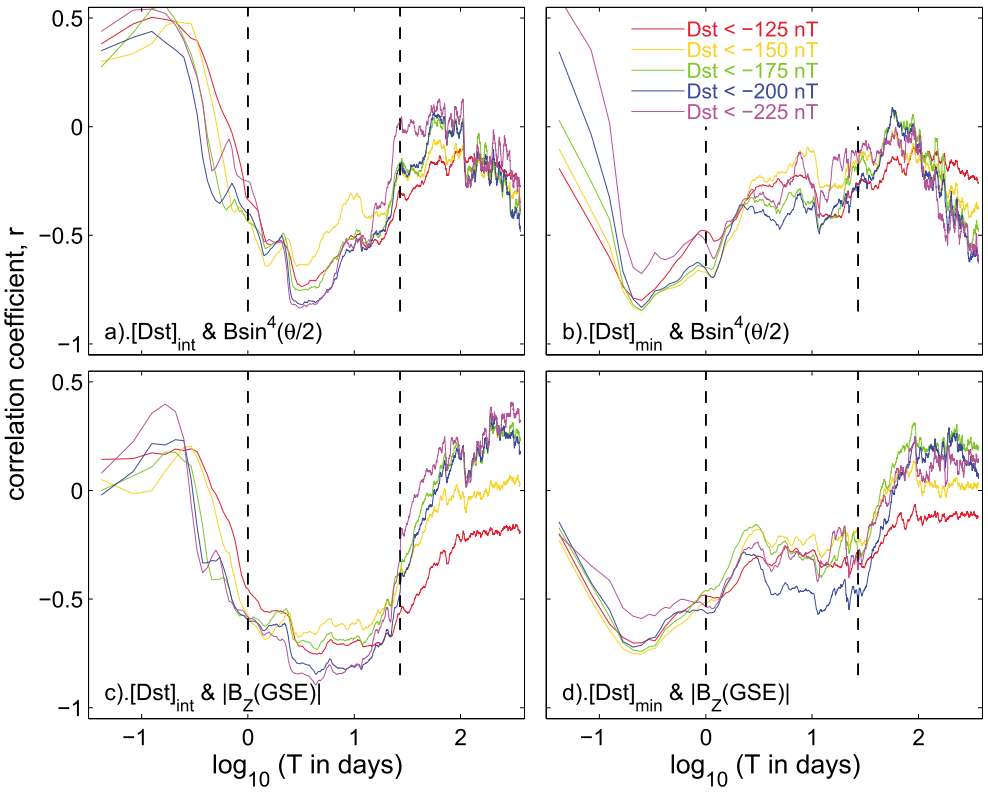

Figure 9. Correlations r between two Dst storm quantifiers and: (a and b) The integral of the IMF coupling function $B\sin^4(\theta/2)$ (where θ is the IMF clock angle in the GSM frame) and (c and d) the integral of the out-of-ecliptic field $|B_z$ (GSE)| over intervals of duration T. In Figure 9a and 9c, the intervals are between ($t_{end} - T$) and t_{end}, where t_{end} is the time of the end of the storm interval and the correlation is with the integrated Dst, $[Dst]_{int}$ over storm intervals defined by $Dst < Dst_o$. In Figure 9b and 9d the intervals are between ($t_{peak} - T$) and t_{peak}, where t_{peak} is the peak of the storm, when $Dst = [Dst]_{min}$, and the correlation is with $[Dst]_{min}$. The various lines are for different Dst thresholds defining the storms: Dst_o: (red) −125 nT, (orange) −150 nT, (green) −175 nT, (blue) −200 nT, and (mauve) −225 nT. The vertical dashed lines are at $T = 1$ day and $T = 27$ days.

This raises the question as to what extent prolonged out-of-ecliptic field matters in driving terrestrial disturbance. Various values of the threshold, Dst_o, were implemented to investigate this: Specifically, Dst_o of − 125 nT, −150 nT, −175 nT, −200 nT, and − 225 nT yielded, respectively, 51, 29, 22, 17, and 11 storms for the 20 year interval studied. Two metrics for the intensity of the storm are employed, similar to those used by *Weigel* [2010]. The first is the minimum Dst reached during the storm, $[Dst]_{min}$ the second is the integral of Dst over the interval when $Dst < Dst_o$ which is termed $[Dst]_{int}$. The former is more useful if the largest disturbance (minimum Dst) is most relevant to the space weather effect under consideration, irrespective of how long the storm lasts. The latter is more useful if the space weather effect is accumulated and integrated over the storm such that its duration matters as well as its maximum amplitude. To evaluate the effect of timescale, we here consider two metrics of the IMF, namely, (i) the southward IMF coupling function in GSM coordinates $< B\sin^4(\theta/2) >_T$ and (ii) the absolute value of the out-of-ecliptic field, $< |B_z(\mathrm{GSE})| >_T$. These are both averaged over an interval of duration T leading up to the end of the storm for the $[Dst]_{int}$ metric and leading up to the peak of the storm for the $[Dst]_{min}$ metric. In other words, for $[Dst]_{int}$ we consider $< |B_z$ (GSE)$| >_T$ and $< B\sin^4(\theta/2) >_T$ over the interval between (t_{end}-T) and t_{end}, where t_{end} is the time of the end of the storm, when Dst has risen back up and is equal to Dst_o. For $[Dst]_{min}$ we consider $< |B_z(\mathrm{GSE})| >_T$ and $< B\sin^4(\theta/2) >_T$ over the interval between (t_{peak} T) and t_{peak}, where t_{peak} is the time of minimum Dst during the storm. Note that T is plotted on a logarithmic scale in Figure 9.

Figure 9a shows the (anti)correlation between $[Dst]_{int}$ and $< B\sin^4(\theta/2) >_T$ as a function of T for the five Dst_o thresholds adopted. Figure 9b is the same for $[Dst]_{min}$. The vertical dashed lines are at $T = 1$ day and $T = 27$ days. The best anticorrelation is for $[Dst]_{int}$ and occurs for the largest storms ($Dst < 200$ nT, blue and

mauve lines). This occurs at $T \approx 3$ days which shows that the duration of intervals of out-of-ecliptic field, as well as their magnitude matters when we consider integrated metrics such as $[Dst]_{int}$. On the other hand, Figure 9b shows that predicting the peak of the storm, $[Dst]_{min}$ is best done with the average of $< B\sin^4(\theta/2) >_T$ over a 6 h interval before the peak.

Figures 9c and 9d repeat this analysis without knowledge of the direction of the field, by using the absolute value of the out-of-ecliptic field, $<|B_z(GSE)| >_T$. This is of interest because from coronal and heliospheric imaging, with MHD modeling of the heliosphere, we may be able to predict the magnitude of the out-of-ecliptic field much more easily than we can predict the southward component. Note that the anticorrelation of $[Dst]_{int}$ and $< |B_z(GSE)| >_T$ is -0.9 at $T = 4.5$ days for the largest storms and such a high correlation has been obtained without any consideration of the polarity of the out-of-ecliptic field. It appears that this is largely because the largest events are caused by flux rope structures, usually containing both northward and southward field and when averages are taken over 4.5 days $|B_z(GSE)|$ is related to the geoeffective component that has $B_z(GSE) < 0$. In addition, event sheaths tend to also contain both polarities of (enhanced) out-of-ecliptic field [*Owens et al.*, 2005]. This means that for the largest disturbances, we may not have to place so much emphasis on predicting the southward component of the IMF, if we are interested in the integrated effect of the storm, $[Dst]_{int}$. (This is true as long as we can accept a relatively small number of false alarms due to "N-type" unipolar clouds containing only northward IMF: Note also that there remain some differences between the responses to north-then-south and south-then-north bipolar clouds [*Fenrich and Luhmann*, 1998; *Kilpua et al.*, 2012].) Figure 9d is the same plot for $|B_z(GSE)|$ and the peak disturbance, $[Dst]_{min}$. In this case peak anticorrelation is found for $T = 6$ h, as for $< B\sin^4(\theta/2) >_T$, but the best correlation is -0.75 (and less for the largest storms). Hence, without knowing the polarity of out-of-ecliptic field, $[Dst]_{min}$ is not as predictable as $[Dst]_{int}$.

In Figures 9b and 9d the peak anticorrelation with $[Dst]_{min}$ is at $T = 6$ h for all cases, i.e., the amplitude of the peak of the storm correlates best with the southward IMF averaged over the previous 6 h. However, using the Fisher Z test [*Lockwood*, 2002], we find that the anticorrelation is not significantly different from its peak value (at the 2σ level) for T between 4 h and T of 12 h. This is the reason why, when searching for the most southward IMF ahead of each storm time hour ($Dst < Dst_o$) in Figure 6, we used the maximum $B\sin^4(\theta/2)$ value in the prior 12 h.

3.4. Identification of ICMEs and CIRs

The OMNI2 data set of hourly solar wind and interplanetary observations is here sorted into various classifications: (1) inside a ICME core; (2) within the sheath ahead of an ICME; (3) within 1.5 days of a CIR or SIR; (4) within 1.5 days of a sector boundary (but with no CIR/SIR nor ICME detected); and (5) quiet solar wind not influenced by CIRs, SIRs, or CMEs but containing small transients (STs), smaller-scale structure, and sector crossings that are not accompanied by an ICME or CIR/SIR. In fact, classification (4) is not used hereafter as it was found to give almost identical results to classification (5): In other words, sector boundaries are not in themselves significant and have relevance only because they tend to be sites where both ICMEs and CIR/SIRs occur.

To define CIRs (and other stream interaction regions, SIRs, which are not necessarily corotating), we use the procedure adopted by *Scott et al.* [2014]. The arrival of high-speed solar wind streams can be inferred from changes in the V_Y(GSE) component of the flow [*McPherron et al.*, 2004; *Denton et al.*, 2009; *Davis et al.*, 2012]. A bipolar V_Y (GSE) signature is formed because the stream interface ahead of the fast flow is generally oriented in the Parker spiral direction and as it is pushed in the $-X$ direction by the fast stream, this generates a flow in the $-Y$ direction ahead of the stream interface. Behind the interface, the fast flow is deflected by the angled interface in the $+Y$ direction. Figure 10 shows a superposed epoch study based on the time t_o when V_Y(GSE) changes from negative to positive and the 5 hour running mean of V_Y(GSE) subsequently exceeds a threshold V_{Yo}. Events that are classified as ICMEs (see below) are excluded. We note the similarity between Figure 10 and the schematic of a typical recurrent storm in Figure 11 of *Tsurutani et al.* [2006]. The value of the threshold V_{Yo} used was varied, and its effects are discussed later in this paper. In Figure 10 $V_{Yo} = 30\,km\,s^{-1}$ was used, which identifies 4885 CIRs/SIRs, which is an average of 18 per solar rotation. If the threshold is raised to $V_{Yo} = 70\,km\,s^{-1}$, just 223 CIRs/SIRs are identified which is an average of 0.8 per solar rotation. Figure 10 (first panel) shows the average variation of V_Y(GSE) as a function of $(t - t_o)$. Figure 10 (second panel) shows that around the time of the

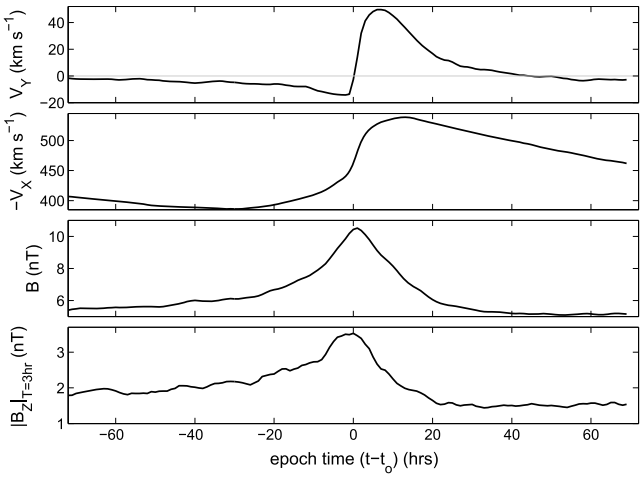

Figure 10. Superposed epoch plot (composite) of average flow and field variations around CIRs/SIRs. Time $t = t_o$ is defined by when the Y component of the solar wind velocity in the GSE frame, V_Y(GSE), changed from negative to positive and the 5 h mean of V_Y(GSE) subsequently (in the next 16 h) exceeded a threshold of $V_{Yo} = +30$ km s^{-1}, but there was no ICMEs present in the catalogue by *Richardson and Cane* [2010] (updated to 1 January 2016). The variations with epoch time ($t - t_o$) are shown for (first panel) V_Y(GSE), the radial solar wind speed away from the Sun, (second panel) $-V_X$(GSE), (third panel) the IMF field strength B, and (fourth panel) the out-of-ecliptic field $|B_Z$(GSE)|.

CIR/SIR, the radial flow speed $-V_X$(GSE) increases and Figure 10 (third panel) shows that the IMF peaks due to the compression by the fast solar wind driver gas seen at $t > t_o$. For the V_{Yo} shown, the average B is enhanced by about 67%. Figure 10 (fourth panel) shows that the out-of-ecliptic field $|B_z$(GSE)| is increased at the time of the CIR/SIR by a comparable fraction, showing the main effect, on average, is due to the compressive effect on B, rather than an orientation change in the field direction. At the end of the plot, $(t - t_o) = 72$ h, $-V_X$(GSE) remains enhanced and $|B_z$(GSE)| (and, to a much smaller degree, B) are depressed, compared to pre-event levels. However, after about $(t - t_o) = 36$ h, the field is reasonably constant, indicating this is a feature of the fast solar wind flow region rather than the transition from slow to fast solar wind (i.e., the CIR/SIR itself). Both B and $-V_X$(GSE) begin to be enhanced at around $(t - t_o) = -36$ h. This was found to be roughly the case independent of the V_{Yo} used, and so we here take the out-of-ecliptic field to have been influenced by the CIR/SIR for all times within 36 h of the CIR/SIR center: However, note that fast and slow solar winds in either side of this interval have different average field properties.

Figure 11 shows the same composite plots for the ICME events identified in the catalogue of *Cane and Richardson* [2003] and *Richardson and Cane* [2010], as updated to the present day in the online list

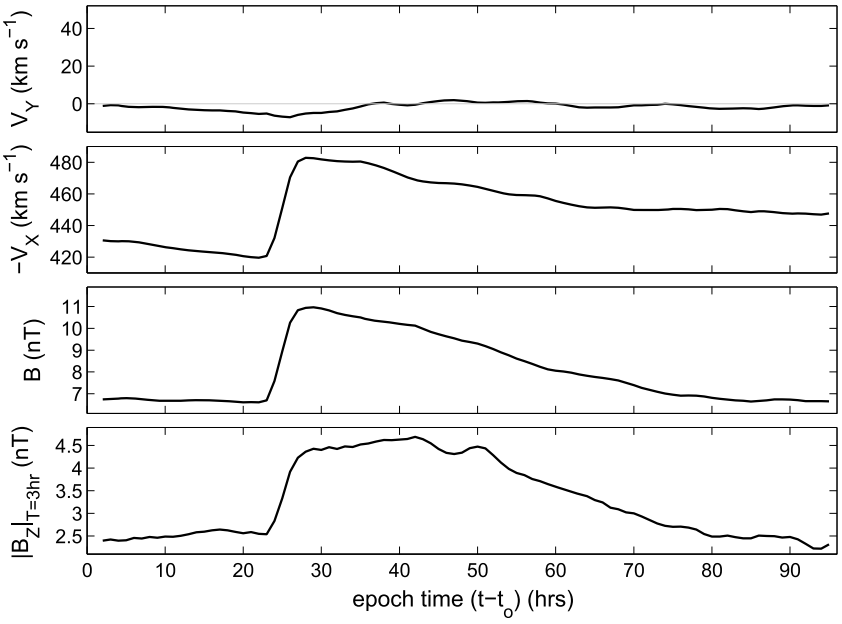

Figure 11. Superposed epoch plot for ICMEs in the same format as Figure 10. Time $t = t_o$ is defined as the start time of ICME particle disturbance upstream of the foreshock in the catalogue by *Richardson and Cane* [2010] (updated to 1 January 2016).

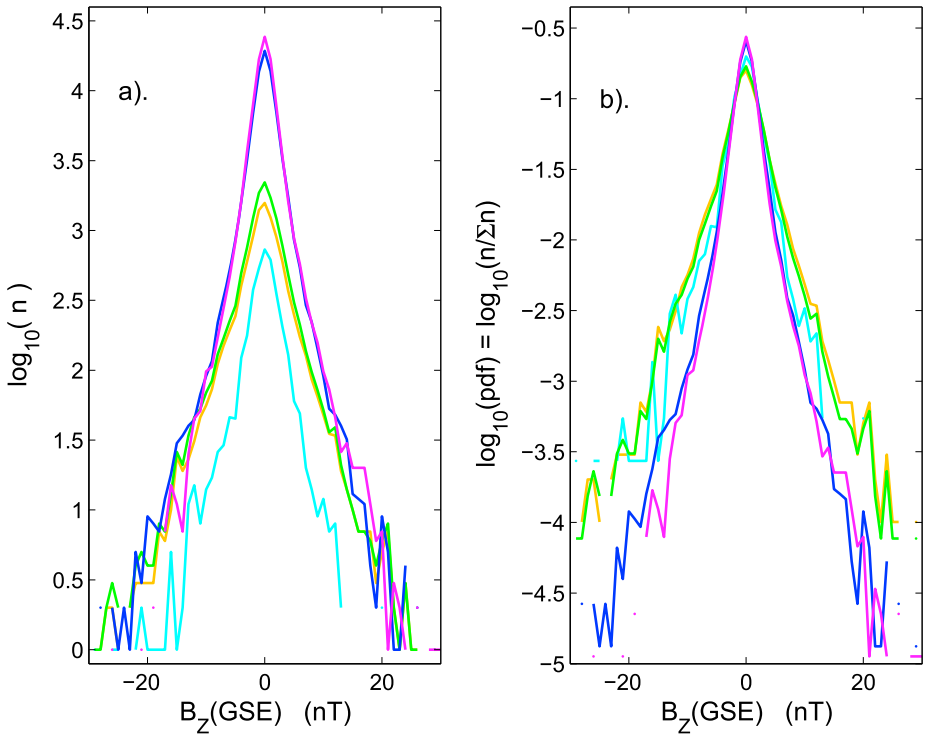

Figure 12. Spectra of hourly B_z(GSE) values for various classifications of the solar wind. (a) The logarithm of the number of hourly values, n, in 1 nT bins for 1996–2015 is shown for (cyan line) within ICME sheaths; (orange line) within ICME cores; (green line) within either part of an ICME; (blue line) within 1.5 days of a CIR/SIR; and (mauve line) outside these definitions of CIRs/SIRs or ICMEs. CIRs/SIRs are here defined as non-ICME events that cause a bipolar V_Y(GSE) signature that exceeds a threshold, V_{Yo}, of +30 km s^{-1}, as in Figure 9. (b) The normalized spectra corresponding to Figure 12a: the logarithm of the pdf, $n/\Sigma n$, is plotted, where the sum is over all B_z(GSE).

(see Acknowledgments for URL). This yields 472 events. To make the plots simple, we take the time t_o for ICMEs to be the estimated start of any ICME-associated disturbance, based primarily on plasma and magnetic field observations [see *Cane and Richardson*, 2003]. This means that some of the gradual decline of the events with increasing $(t - t_o)$ will be caused by the variation in the durations of events; however, as the shock, sheath, and entry into the event core follow relatively quickly after this onset time, these features are less smeared out for this choice of t_o. Figure 10 (first panel) shows that ICMEs also drive a bipolar signature in V_Y(GSE), but it is much weaker, on average, than for the CIRs/SIRs for the set defined here; however, we note that some ICME sheaths contain large V_Y(GSE) flow deflections [*Owens and Cargill*, 2004]. Figure 10 (second panel) shows the driver plasma with increased $-V_X$(GSE) within the event, and Figure 10 (third and fourth panels) shows the average enhancements in B and $|Bz(GSE)|$ during the events. In these ICMEs, the average rise in B is of order 60% whereas that in $|Bz(GSE)|$ is about 125% showing that changes in field orientation contribute considerably to the out-of-ecliptic field during these events. Using the ICME catalogue timings and classifications, we also distinguish between ICME event cores and the ICME sheaths ahead of them.

4. The Spectra of Out-of-Ecliptic Fields

4.1. Occurrence Spectra in Hourly Data for Different Regions

Figure 12a shows the spectra of out-of-ecliptic field in the various types of solar wind discussed in the previous section. The number of hourly means ($T = 1$ h), n, giving $< B_z(GSE) >_T$ falling in bins of width dB_z (GSE) = 1 nT, is plotted on a logarithmic scale as a function of B_z(GSE) for the various classifications of the solar wind. The cyan line is for within ICME sheaths: n is relatively low because these sheath regions are not extensive and pass over the satellites relatively quickly. The orange line is for within ICME cores; the n values are higher because these regions are more extensive than the sheath regions but the shape of the spectrum is similar, and hereafter, we combine ICME sheaths and cores into a single ICME category, the spectrum for

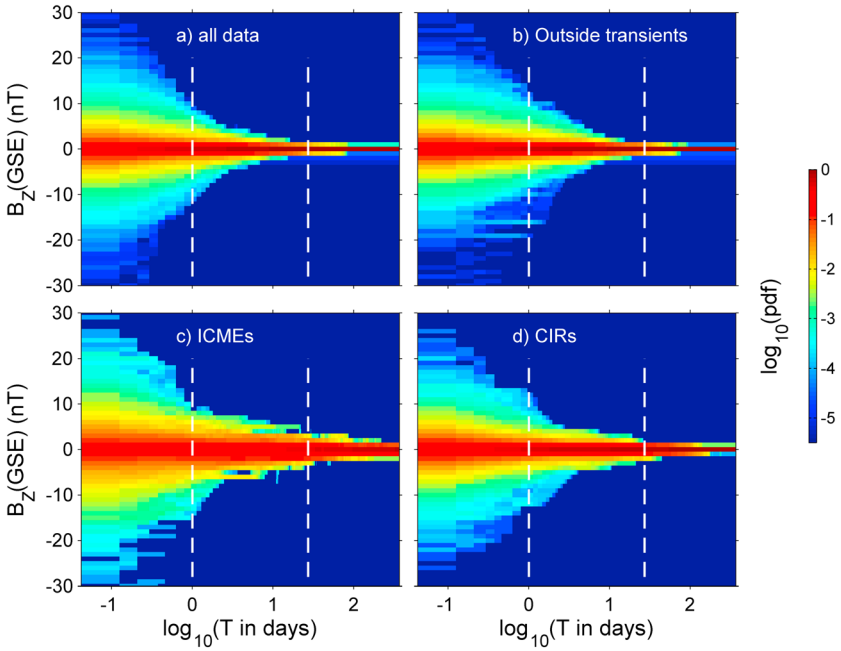

Figure 13. Spectrograms showing the variation of B_z(GSE) spectra with averaging timescale, T, for data from between 1 January 1976 and 1 January 2016. The normalized pdfs are shown as a function of B_z(GSE) and T for (a) all data; (b) all data outside CIRs/SIRs and ICMEs; (c) within ICMEs (sheaths and cores); and (d) within 3 days of a CIR/SIR in the same interval, CIRs/SIRs being defined by the V_Y(GSE) threshold of $V_{Yo} = +30$ km s^{-1} used in Figures 10 and 12. The vertical dashed white lines are at $T = 1$ day and $T = 27$ days.

which is shown by the green line. The blue line is for within 1.5 days of a CIR/SIR, here defined using the V_Y (GSE) threshold $V_{Yo} = +30$ km s^{-1}, as in Figure 10. Lastly, the mauve line is for "quiet" solar wind outside both CIRs/SIRs and ICMEs for the above definitions.

Figure 12b presents the same spectra, using the same line colors, after normalization: That is, the logarithm of the probability density function (pdf) is plotted, $n/\Sigma n$, where the sum is over all B_z(GSE) for that classification. This shows that the pdfs for ICMEs are broader, with a higher occurrence frequency within the events of large out-of-ecliptic field than for CIRs or the quiet solar wind. However, note that the tails of the distributions in Figure 12a are very similar for the mauve, blue, and green lines, showing that when convolved with the occurrence rate of the solar wind classification, both the quiet solar wind and CIRs/SIRs yield as many hours of large out-of-ecliptic field as do ICMEs.

4.2. Effect of Timescale on Occurrence Spectra

Figure 12 is only for hourly averaged data, which is not the relevant timescale for all terrestrial disturbance indices. Figure 13 investigates the effect of averaging timescale T on these spectra. Note that as T is increased, it rises above the durations of the transient events (CIRs/SIRs and ICMEs), and subsequently, the changes in mean values become caused by averaging successive events together. Each vertical slice in each panel of Figure 13 is a pdf spectrum, i.e., $n/\Sigma n$, as shown in Figure 12b for the case of $T = 1$ h. The averaging timescale T is varied from 1 h to 1 year, in quantized quasi-logarithmic steps. The horizontal T scale is logarithmic with the left-hand edge being for $T = 1$ h and the right-hand edge for $T = 1$ year. The vertical dashed white lines are at $T = 1$ day and $T = 27$ days (the latter being the mean solar rotation period, as seen from Earth). In all cases, as expected, the width of the B_z(GSE) spectrum shrinks with increasing T, until it is close to a delta function at $T = 1$ year. However, the various classifications do not behave in the same way. The most important feature is that the distribution remains broader with increasing T for within ICMEs. This provides an explanation why ICMEs are the best drivers of storms with the largest integrated Dst values, $[Dst]_{int}$. Figure 9c shows that $[Dst]_{int}$ correlates best with $< |B_z(\text{GSE})| >_T$ for $T \approx 4.5$ days and Figure 13c shows that at this T, ICMEs provide the broadest distribution, i.e., the largest out-of-ecliptic field (both northward and southward). The reason for this is the persistence of the field, as demonstrated by Figure 14. Figure 14 (top) subdivides the acf of the Z

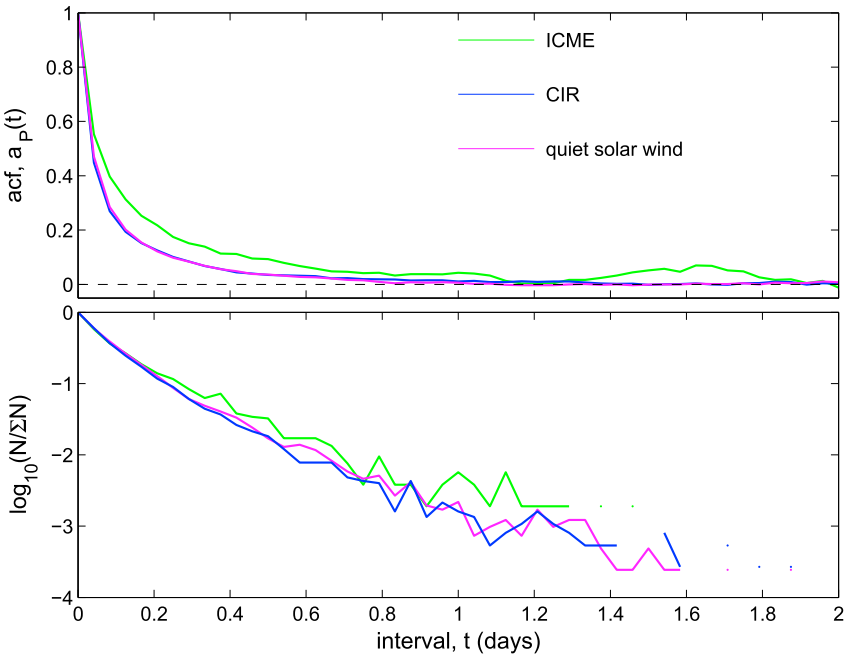

Figure 14. Effects of timescale on the IMF B_Z(GSE) component for three classifications of the solar wind. (top) The autocorrelation function $a_P(t)$ of the polarity of B_z(GSE), P_z(GSE), as a function of lag, t. (bottom) The logarithm of the normalized number of intervals, N, of constant southward polarity P_z(GSE) < 0 lasting between t and $t + dt$ for dt of 1 h, $\log_{10}(N/\Sigma N)$, as a function of t. In Figure 14 (top and bottom), the green line is for within ICMEs, the blue line is for within 1.5 days of a CIR/SIR (defined using $V_{Yo} = 30\,km\,s^{-1}$), and the mauve line is for the quiet solar wind, outside of CIRs, SIRs, and ICMEs.

field polarity P_Z(GSE), $a_P(t)$ (that was shown in Figure 8a) into the various solar wind classifications. These acfs are generated by only including pairs of data points at a given lag where both the original and lagged data series have the required classification (ICME, CIR/SIR, or quiet solar wind). The green line is for within ICMEs and $a_P(t)$ is seen to be broader than for within CIRs/SIRs and for the quiet solar wind. Figure 14 (bottom) corresponds to Figure 8 (bottom) and shows the durations of intervals of constant southward IMF polarity for the three classifications. To compare the distributions, the number of intervals N has been normalized by the total number of intervals for that classification, ΣN. Note that $(N/\Sigma N)$ is again plotted on a logarithmic scale. Although there is very little difference between the distributions for the shorter intervals, there are proportionally more long intervals of constant IMF B_Z polarity within ICMEs. In terms of overall occurrence, Figure 12a shows that CIRs and the quiet solar wind provide as many hours of large out-of-ecliptic field but Figures 13 and 14 show that they are not as continuous as they are within ICMEs and it is this longevity of intervals of large southward IMF that makes ICMEs more geoeffective. This is consistent with the conclusions of *Kozyra et al.* [2006] and *Turner et al.* [2009] who invoked the more sustained nature of forcing as the reason why CIR storms are generally larger than CME storms for a given total energy input into the magnetosphere.

4.3. Origins of Out-of-Ecliptic Field in the Quiet Solar Wind

The large number of hours in the quiet solar wind showing large out-of-ecliptic field, as demonstrated by Figure 12a, is a surprise, and it is worth investigating their origin. The previous section shows that despite the magnitude of the out-of-ecliptic IMF, the southward directed field in this classification is much less geoeffective because it persists for shorter intervals, which means that it originates from smaller-scale structure. Figure 15 studies the effect of the V_Y(GSE) threshold used to define CIRs/SIRs, V_{Yo}, on the CIR/SIR spectrum shown in Figure 12a. The various blue lines are for the labeled V_{Yo} thresholds which have been varied between $10\,km\,s^{-1}$ and $80\,km\,s^{-1}$. It is apparent that as V_{Yo} is reduced, more CIRs/SIRs are defined, and the sample numbers n increase. Not as expected is that the shape of the distribution remains the same and that shape is the same as the distribution for the quiet solar wind (shown in mauve in Figure 15 for $V_{Yo} = 30\,km\,s^{-1}$). In general, the n values for the quiet solar wind fall a little as V_{Yo} is decreased and more

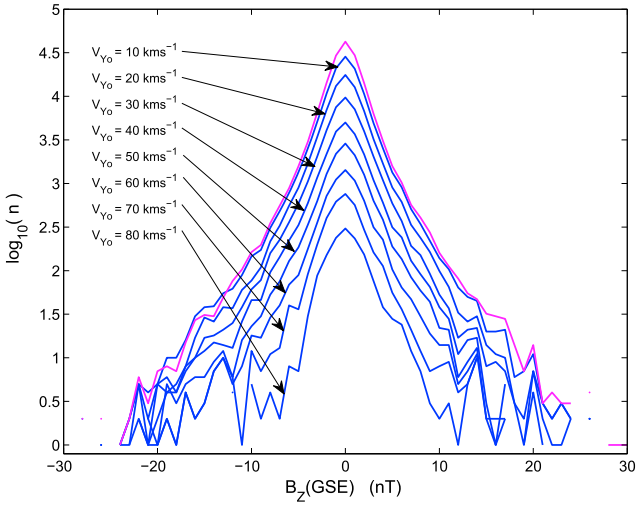

Figure 15. The effect of the V_Y(GSE) threshold, V_{Yo}. The blue lines are the hourly B_Z(GSE) spectra for within 3 days of a CIR/SIR defined by a bipolar V_Y(GSE) signature that exceeds a threshold, V_{Yo}, which is here varied between +10 km s^{-1} and +80 km s^{-1} . The mauve line is the spectra outside CIRs, SIRs, or ICMEs, as shown in Figure 12: this is for V_{Yo} = +30 km s^{-1} and is only very weakly dependent on V_{Yo} for the logarithmic scale of n used.

hourly means are classed as being within a CIR/SIR rather than the quiet solar wind. However, the long intervals spent in the quiet solar wind make this effect small (i.e., there is only a small fractional drop in n) and for the log$_{10}$(n) scale used, the difference cannot be seen for V_{Yo} between 30 km s^{-1} and 80 km s^{-1}. For V_{Yo} below 30 km s^{-1}, the decrease in n can be detected but the shape (the normalized spectrum) remains the same (not shown). Hence, it appears that the quiet solar wind spectrum is largely caused by small stream-stream interactions (at least as they are seen at 1 AU, they may have been larger closer to the Sun and decayed).

4.4. Relationship of Out-of-Ecliptic Field and Deviations From Parker Spiral

Heliospheric effects such as ICMEs and stream-stream interactions drive out-of-ecliptic field by deflecting the heliospheric magnetic field in the north-south (elevation) direction, but they also cause deviations from Parker spiral field by deflecting the field orientation in the azimuthal direction. Just as the out-of-ecliptic field tends to zero as increasingly longer averaging timescales are used, so the field orientation tends to that predicted by Parker spiral theory [*Hapgood et al.*, 1991]. Figure 16 analyzes the

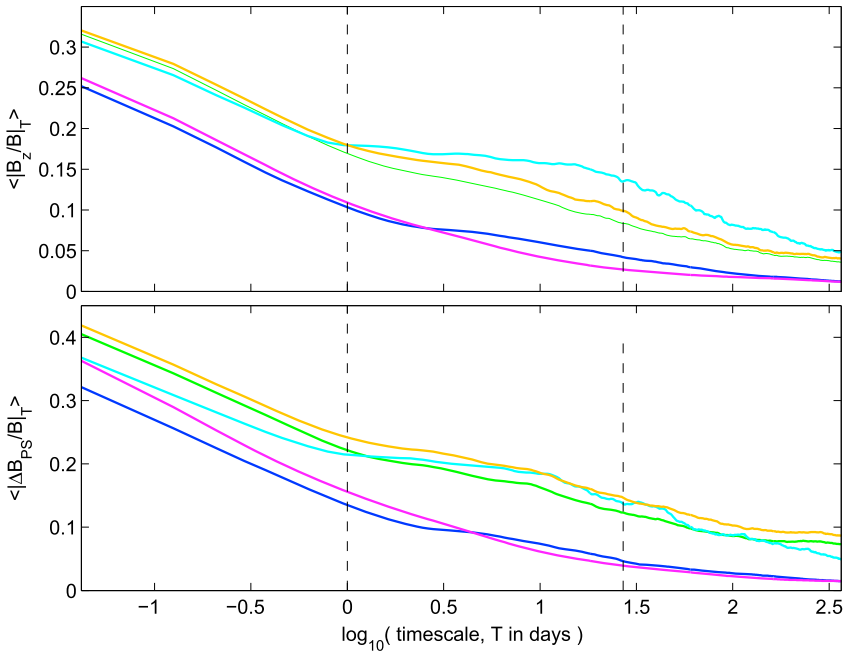

Figure 16. (top) The mean normalized out-of-ecliptic field component $< |B_z(\mathrm{GSE})/B| >_T$ and (bottom) the mean normalized in-ecliptic IMF component orthogonal to the predicted Parker spiral direction $< |\Delta B_{PS}/B| >_T$. Both are shown as a function of averaging timescale T. The line colors are as in Figure 13: (cyan) inside ICME sheaths; (orange line) inside ICME cores; (green line) in ICMEs, (blue line) within 3 days of a CIR/SIR; and (mauve line) outside CIRs, SIRs or ICMEs. CIRs/SIRs are here defined as non-ICME events that cause a bipolar V_Y(GSE) signature that exceeds a threshold, V_{Yo}, of +30 km s^{-1}, as in Figure 10. The vertical dashed lines are at T = 1 day and T = 27 days.

variation of both elevational and azimuthal IMF deviations with timescale T for the various types of solar wind considered here. Figure 16 (top) shows the mean value of $<|B_z(\mathrm{GSE})|/B>_T$ as a function of T, Figure 16 (bottom) shows the field component normal to the predicted Parker spiral field direction (for the prevailing solar wind speed), again as a ratio of the IMF magnitude, $<\Delta B_{PS}/B>_T$. The color coding of the lines are as used in Figure 12. The most important feature is that the behavior in the two parts of Figure 16 (top and bottom) is very similar. The plot for CIRs/SIRs (blue line) is for the threshold $V_{Yo} = 30\ \mathrm{km\ s^{-1}}$, other thresholds are not shown, but for lower V_{Yo} the blue lines in Figure 16 (top and bottom) get even closer to the mauve lines which are for the quiet solar wind classification. The main effect of increasing V_{Yo} is to make the leveling out at T between 1 and 27 days more pronounced. This is because for higher V_{Yo} the selection tends toward, at most, one event per solar rotation. This feature can be detected in the ICME behavior because for quieter intervals many solar rotations contain just one ICME.

5. Discussion and Conclusions

Geometric factors, controlled by the position of the Earth in its annual orbit (through the tilt of Earth rotational axis) and by the universal time (through its rotation and the offset of the geomagnetic and rotational axes), influence the geoeffectiveness of the solar wind on the terrestrial magnetosphere, ionosphere, and thermosphere. However, we have demonstrated that their effects are limited and the largest storms are mainly caused by large out-of-ecliptic IMF embedded in the solar wind flow with relatively minor influence of the dipole tilt effects. Some smaller storms are caused by large out-of-ecliptic IMF, with a secondary influence of the dipole tilt effects and these tend to be more common around the equinoxes This causes the characteristic signature of the R-M effect in the IMF B_Y/t-o-y behavior of the average *Dst* index, a signature that can be seen in the numbers of smaller *Dst* storms but is hardly detected in the corresponding behavior for larger storms.

The quiet solar wind and CIRs/SIRs both give as many hours of strongly out-of-ecliptic IMF, and hence strongly southward IMF, as do ICME transits. This is true for any quantitative definition of the word "strong." It is somewhat surprising that ICMEs, sheaths, and SIR/CIRs show such similar spectra of hourly averaged IMF $|B_z|$ and that the total number of hours of large $|B_z|$ is a great in the quiet solar wind as in transient events and around stream-stream interfaces. It is well documented that nearly all intense storms are related to ICMEs [e.g., *Huttunen et al*., 2002; *Richardson and Cane*, 2012], and we here provide evidence that this is because within ICMEs the IMF tends to remain consistently southward, rather than fluctuating rapidly in polarity. The sustained southward IMF would allow magnetospheric convection to increase strongly and steadily and to build up the ring current. For CIRs/SIRs the sustained out-of-ecliptic field means that although they are generally less geoeffective than ICMEs, they have a greater effect than might have been expected [*Kozyra et al*., 2006; *Turner et al*., 2009]. Hence, we have presented evidence that ICMEs are more geoeffective in terms of enhancing *Dst*, not because they contain stronger southward IMF but because that strong southward IMF is more persistent and longer lived and this is consistent with how the ring current is enhanced during storms.

The spectrum for CIRs/SIRs converges with that of the quiet solar wind as the threshold of the Y component of the solar wind speed, used to define CIRs/SIRs, is reduced. From this we conclude that weaker stream-stream interactions are the dominant driver of out-of-ecliptic field in the quiet solar wind. We also show that for all classes of the solar wind, the variation of the out-of-ecliptic field with averaging timescale is the same as the variation of the field component normal to the predicted Parker spiral field direction. This strongly suggests that the out-of-ecliptic field shares the same origin as the deviation of the field from Parker spiral orientation.

The effect of timescale explains why the response of the *Dst* index and of ring current injections is, essentially, axial in its time-of-day/time-of-year pattern, while the solar wind forcing has a Russell-McPherron pattern. The equinoctial pattern is seen only for features which respond strongly to the substorm current wedge in substorm expansion phases because it is formed by processes influencing the near tail and/or aurora ionospheric electrojet and not by an equinoctial effect on magnetopause reconnection, as was demonstrated by *Finch et al.* [2008]. This supports the concept of *Lyatsky et al.* [2001] that the equinoctial pattern in range-based geomagnetic indices is associated with the solar illumination of one of the auroral electrojets rather than an effect on dayside magnetopause reconnection voltage, although it does not eliminate the possibility of an effect of the UT variation in the tail "hinge" angle [*Kivelson and Hughes*, 1990]. The axial pattern for

moderate-to-large *Dst* perturbations is shown to be consistent with the R-M forcing, and the effect of the longer timescale over which the forcing needs to persist to give a major *Dst* disturbance. The out-of-ecliptic field (irrespective of its north/south polarity) has exceptionally high correlation with the subsequent integrated *Dst* response for averaging timescales of 4–5 days: A feature which could be very useful for operation predictions of storms and their effects.

Acknowledgments
This work was stimulated by discussions at the second SEREN workshop on the evolution of the geoeffective heliospheric magnetic field, held at Steventon, Abingdon, UK on 2–4 December 2015. We thank M.A. Hapgood, M.M. Bisi, and R.A. Harrison of RAL Space for organizing the meeting. The authors are grateful to the staff of Space Physics Data Facility, NASA/Goddard Space Flight Centre, who prepared and made available the OMNI2 data set used. The data were downloaded from http://omniweb.gsfc.nasa.gov/ow.html. We are also most grateful to Ian Richardson of NASA Goddard Space Flight Center and University of Maryland, USA, and Hilary Cane of the University of Tasmania, Australia for compiling, maintaining and making available the list of near-Earth interplanetary coronal mass ejections since January 1996, which is available from http://www.srl.caltech.edu/ACE/ASC/DATA/level3/icmetable2.htm. The work is supported by STFC consolidated grant ST/M000885/1.

References

Alexeev, I. I., E. S. Belenkaya, V. V. Kalegaev, Y. I. Feldstein, and A. Grafe (1996), Magnetic storms and magnetotail currents, *J. Geophys. Res.*, *101*, 7737–7747, doi:10.1029/95JA03509.

Alves, M. V., E. Echer, and W. D. Gonzalez (2006), Geoeffectiveness of corotating interaction regions as measured by *Dst* index, *J. Geophys. Res.*, *111*, A07S05, doi:10.1029/2005JA011379.

Baker, D. N., R. D. Zwickl, S. J. Bame, E. W. Hones Jr., B. T. Tsurutani, E. J. Smith, and S.-I. Akasofu (1983), An ISEE 3 high time resolution study of interplanetary parameter correlations with magnetospheric activity, *J. Geophys. Res.*, *88*, 6230–6242, doi:10.1029/JA088iA08p06230.

Balan, N., R. Skoug, S. Tulasi Ram, P. K. Rajesh, K. Shiokawa, Y. Otsuka, I. S. Batista, Y. Ebihara, and T. Nakamura (2015), CME front and severe space weather, *J. Geophys. Res. Space Physics*, *119*, 10,041–10,058, doi:10.1002/2014JA020151.

Borovsky, J. E., and M. H. Denton (2006), Differences between CME-driven storms and CIR-driven storms, *J. Geophys. Res.*, *111*, A07S08, doi:10.1029/2005JA011447.

Borovsky, J. E., and M. H. Denton (2010), Magnetic field at geosynchronous orbit during high-speed stream-driven storms: Connections to the solar wind, the plasma sheet, and the outer electron radiation belt, *J. Geophys. Res.*, *115*, A08217, doi:10.1029/2009JA015116.

Borovsky, J. E., M. F. Thomsen, and R. C. Elphic (1998), The driving of the plasma sheet by the solar wind, *J. Geophys. Res.*, *103*, 17,617–17,639, doi:10.1029/97JA02986.

Bothmer, V., and R. Schwenn (1998), The structure and origin of magnetic clouds in the solar wind, *Ann. Geophys.*, *16*(1), 1–24, doi:10.1007/s00585-997-0001-x.

Bruno, R., and V. Carbone (2013), The solar wind as a turbulence laboratory, *Living Rev. Solar Phys.*, *10*, doi:10.12942/lrsp-2013-2.

Bruno, R., V. Carbone, P. Veltri, E. Pietropaolo, and B. Bavassano (2001), Identifying intermittency events in the solar wind, *Planet. Space Sci.*, *49*, 1201–1210, doi:10.1016/S0032-0633(01)00061-7.

Burlaga, L., E. Sittler, F. Mariani, and R. Schwenn (1981), Magnetic loop behind an interplanetary shock: Voyager, Helios, and IMP 8 observations, *J. Geophys. Res.*, *86*, 6673–6684, doi:10.1029/JA086iA08p06673.

Burton, R. K., R. L. McPherron, and C. T. Russell (1975), An empirical relationship between interplanetary conditions and *Dst*, *J. Geophys. Res.*, *80*, 4204–4214, doi:10.1029/JA080i031p04204.

Cane, H. V., and I. G. Richardson (2003), Interplanetary coronal mass ejections in the near-Earth solar wind during 1996–2002, *J. Geophys. Res.*, *108*(A4), 1156. doi:10.1029/2002JA009817.

Cliver, E. W., Y. Kamide, and A. G. Ling (2000), Mountains versus valleys: Semiannual variation of geomagnetic activity, *J. Geophys. Res.*, *105*, 2413–2424, doi:10.1029/1999JA900439.

Cowley, S. W. H. (1982), The causes of convection in the Earth's magnetosphere: A review of developments during the IMS, *Rev. Geophys.*, *20*, 531–565, doi:10.1029/RG020i003p00531.

Cowley, S. W. H. (1991), Acceleration and heating of space plasmas—Basic concepts, *Ann. Geophys.*, *9*, 176–187.

Cowley, S. W. H., and M. Lockwood (1992), Excitation and decay of solar-wind driven flows in the magnetosphere-ionosphere system, *Ann. Geophys.*, *10*, 103–115.

Cramer, W. D., N. E. Turner, M.-C. Fok, and N. Y. Buzulukova (2013), Effects of different geomagnetic storm drivers on the ring current: CRCM results, *J. Geophys. Res. Space Physics*, *118*, 1062–1073, doi:10.1002/jgra.50138.

Crooker, N. U., and E. W. Cliver (1994), Postmodern view of M-regions, *J. Geophys. Res.*, *99*, 23,383–23,390, doi:10.1029/94JA02093.

Crooker, N. U., and G. L. Siscoe (1986), On the limits of energy transfer through dayside merging, *J. Geophys. Res.*, *91*, 13,393–133,397, doi:10.1029/JA091iA12p13393.

Crooker, N. U., E. W. Cliver, and B. T. Tsurutani (1992), The semiannual variation of great geomagnetic storms and the postshock Russell-McPherron effect preceding coronal mass ejecta, *Geophys. Res. Lett.*, *19*, 429–432, doi:10.1029/92GL00377.

Crooker, N. U., J. T. Gosling, and S. W. Kahler (1998), Magnetic clouds at sector boundaries, *J. Geophys. Res.*, *103*, 301–306, doi:10.1029/97JA02774.

Davis, C. J., J. A. Davies, M. Lockwood, A. P. Rouillard, C. J. Eyles, and R. A. Harrison (2009), Stereoscopic imaging of an Earth-impacting solar coronal mass ejection: A major milestone for the STEREO mission, *Geophys. Res. Lett.*, *36*, L08102, doi:10.1029/2009GL038021.

Davis, C. J., J. A. Davies, M. J. Owens, and M. Lockwood (2012), Predicting the arrival of high-speed solar wind streams at Earth using the STEREO Heliospheric Imagers, *Space Weather*, *10*, S0200, doi:10.1029/2011SW000737.

Denton, M. H., J. E. Borovsky, R. M. Skoug, M. F. Thomsen, B. Lavraud, M. G. Henderson, R. L. McPherron, J. C. Zhang, and M. W. Liemohn (2006), Geomagnetic storms driven by ICME- and CIR-dominated solar wind, *J. Geophys. Res.*, *111*, A07S07, doi:10.1029/2005JA011436.

Denton, M. H., T. Ulich, and E. Tutunen (2009), Modification of mid-latitude ionospheric parameters in the F_2 layer by persistent high-speed solar wind streams, *Space Weather*, *7*, S04006, doi:10.1029/2008SW000443.

Dungey, J. W. (1961), Interplanetary magnetic field and the auroral zones, *Phys. Rev. Lett.*, *6*, 47–48, doi:10.1103/PhysRevLett.6.47.

Echer, E., and W. D. Gonzalez (2004), Geoeffectiveness of interplanetary shocks, magnetic clouds, sector boundary crossings and their combined occurrence, *Geophys. Res. Lett.*, *31*, L09808, doi:10.1029/2003GL019199.

Echer, E., W. D. Gonzalez, and B. T. Tsurutani (2008), Interplanetary conditions leading to superintense geomagnetic storms (*Dst* $>$ 250 nT) during solar cycle 23, *Geophys. Res. Lett.*, *35*, L06S03, doi:10.1029/2007GL031755.

Etemadi, A., S. W. H. Cowley, M. Lockwood, B. J. I. Bromage, D. M. Willis, and H. Lühr (1988), The dependence of high-latitude dayside ionospheric flows on the north-south component of the IMF: A high time resolution correlation analysis using EISCAT "POLAR" and AMPTE UKS and IRM data, *Planet. Space Sci.*, *36*, 471–498, doi:10.1016/0032-0633(88)90107-9.

Fenrich, F. R., and J. G. Luhmann (1998), Geomagnetic response to magnetic clouds of different polarity, *Geophys. Res. Lett.*, *25*, 2999–3002, doi:10.1029/98GL51180.

Finch, I. D., and M. Lockwood (2007), Solar wind-magnetosphere coupling functions on timescales of 1 day to 1 year, *Ann. Geophys.*, *25*, 495–506, doi:10.5194/angeo-25-495-2007.

Finch, I. D., M. Lockwood, and A. P. Rouillard (2008), The effects of solar wind magnetosphere coupling recorded at different geomagnetic latitudes: Separation of directly-driven and storage/release systems, *Geophys. Res. Lett.*, *35*, L21105, doi:10.1029/2008GL035399.

Fujiwara, H., S. Maeda, H. Fukunishi, T. J. Fuller-Rowell, and D. S. Evans (1996), Global variations of thermospheric winds and temperatures caused by substorm energy injection, *J. Geophys. Res.*, *101*, 225–239, doi:10.1029/95JA01157.

Gonzalez, W. D., B. T. Tsurutani, and A. L. Clúa de Gonzalez (1999), Interplanetary origin of geomagnetic storms, *Space Sci. Rev.*, *88*(3–4), 529–562, doi:10.1023/A:1005160129098.

Gosling, J. T. (1993), The solar flare myth, *J. Geophys. Res.*, *98*, 18,937–18,949, doi:10.1029/93JA01896.

Gosling, J. T., and V. J. Pizzo (1999), Formation and evolution of corotating interaction regions and their three dimensional structure, *Space Sci. Rev.*, *89*, 21–52, doi:10.1007/978-94-017-1179-1_3.

Gosling, J. T., D. J. McComas, J. L. Phillips, and S. J. Bame (1991), Geomagnetic activity associated with earth passage of interplanetary shock disturbances and coronal mass ejections, *J. Geophys. Res.*, *96*, 7831–7839, doi:10.1029/91JA00316.

Hapgood, M. A. (1992), Space physics coordinate transformations: A user guide Space physics coordinate transformations: A user, *Planet. Space Sci.*, *40*(5), 711–717, doi:10.1016/0032-0633(92)90012-D.

Hapgood, M. A., G. Bowe, M. Lockwood, D. M. Willis, and Y. Tulunay (1991), Variability of the interplanetary magnetic field at 1 A.U. over 24 years: 1963–1986, *Planet. Space Sci.*, *39*, 411–423, doi:10.1016/0032-0633(91)90003-S.

Horbury, T. S., D. Burgess, M. Fränz, and C. J. Owen (2001), Three spacecraft observations of solar wind discontinuities, *Geophys. Res. Lett.*, *28*, 677–680, doi:10.1029/2000GL000121.

Huttunen, K. E. J., H. E. J. Koskinen, and R. Schwenn (2002), Variability of magnetospheric storms driven by different solar wind perturbations, *J. Geophys. Res.*, *107*(A7), 1121, doi:10.1029/2001JA900171.

Jones, G. H., A. Rees, A. Balogh, and R. J. Forsyth (2002), The draping of heliospheric magnetic fields upstream of coronal mass ejecta, *Geophys. Res. Lett.*, *29*(11), 1520, 15/1–15/4, doi:10.1029/2001GL014110.

Jordanova, V. K., D. T. Welling, S. G. Zaharia, L. Chen, and R. M. Thorne (2012), Modeling ring current ion and electron dynamics and plasma instabilities during a high-speed stream driven storm, *J. Geophys. Res.*, *117*, A00L08, doi:10.1029/2011JA017433.

Kane, R. P. (2005), How good is the relationship of solar and interplanetary plasma parameters with geomagnetic storms?, *J. Geophys. Res.*, *110*, A02213, doi:10.1029/2004JA010799.

Kilpua, E. K. J., et al. (2009), Small solar wind transients and their connection to the large-scale coronal structure, *Solar Phys.*, *256*, 327–344, doi:10.1007/s11207-009-9366-1.

Kilpua, E. K. J., Y. Li, J. G. Luhmann, L. K. Jian, and C. T. Russell (2012), On the relationship between magnetic cloud field polarity and geoeffectiveness, *Ann. Geophys.*, *30*, 1037–1050, doi:10.5194/angeo-30-1037-2012.

King, J. H., and N. E. Papitashvili (1994), Interplanetary medium data book, Suppl. 5, 1988–1993, NSSDC/WDC-A-R&S 94-08, NASA/Natl. Space Sci. Data Center, GSFC, Greenbelt, Md.

King, J. H., and N. E. Papitashvili (2005), Solar wind spatial scales in and comparisons of hourly Wind and ACE plasma and magnetic field data, *J. Geophys. Res.*, *110*, A02104, doi:10.1029/2004JA010649.

Kivelson, M. G., and W. J. Hughes (1990), On the threshold for triggering substorms, *Planet. Space Sci.*, *38*, 211–220, doi:10.1016/0032-0633(90)90085-5.

Konradi, A., C. L. Semar, and T. A. Fritz (1975), Substorm-injected protons and electrons and the injection boundary model, *J. Geophys. Res.*, *80*(4), 543–552, doi:10.1029/JA080i004p00543.

Kozyra, J. U., et al. (2006), Response of the upper/middle atmosphere to coronal holes and powerful high-speed solar wind streams in 2003, in *Recurrent Magnetic Storms: Corotating Solar Wind Streams*, *Geophys. Monogr. Ser.*, vol. 167, edited by B. T. Tsurutani et al., pp. 319–340, AGU, Washington, D. C.

Lavraud, B., M. F. Thomsen, J. E. Borovsky, M. H. Denton, and T. I. Pulkkinen (2006), Magnetosphere preconditioning under northward IMF: Evidence from the study of coronal mass ejection and corotating interaction region geoeffectiveness, *J. Geophys. Res.*, *111*, A09208, doi:10.1029/2005JA011566.

Lockwood, M. (2002), An evaluation of the correlation between open solar flux and total solar irradiance, *Astron. Astrophys.*, *382*, 678–687, doi:10.1051/0004-6361:20011666.

Lockwood, M. (2004), Solar Outputs, their variations and their effects of Earth, in *The Sun, Solar Analogs and the Climate, Proc. Saas-Fee Advanced Course (15-20 March, 2004, Davos, Switzerland)*, vol. 34, edited by J. D. Haigh et al., pp. 107–304, Springer, Berlin.

Lockwood, M. (2013), Reconstruction and prediction of variations in the open solar magnetic flux and interplanetary conditions, *Living Rev. Solar Physics*, doi:10.12942/lrsp-2013-4.

Lockwood, M., and C. J. Davis (1996), On the longitudinal extent of magnetopause reconnection bursts, *Ann. Geophys.*, *14*, 865–878, doi:10.1007/s00585-996-0865-1.

Lockwood, M., and M. J. Owens (2014), Implications of the recent low solar minimum for the solar wind during the Maunder minimum, *Astrophys. J. Lett.*, *781*, L7, doi:10.1088/2041-8205/781/1/L7.

Lockwood, M., S. W. H. Cowley, and M. P. Freeman (1990), The excitation of plasma convection in the high latitude ionosphere, *J. Geophys. Res.*, *95*, 7961–7971, doi:10.1029/JA095iA06p07961.

Lockwood, M., R. Stamper, and M. N. Wild (1999), A doubling of the sun's coronal magnetic field during the last 100 years, *Nature*, *399*, 437–439, doi:10.1038/20867.

Lockwood, M., M. R. Hairston, I. D. Finch, and A. P. Rouillard (2009), Transpolar voltage and polar cap flux during the substorm cycle and steady convection events, *J. Geophys. Res.*, *114*, A01210, doi:10.1029/2008JA013697.

Lockwood, M., H. Nevanlinna, L. Barnard, M. J. Owens, R. G. Harrison, A. P. Rouillard, and C. J. Scott (2014), Reconstruction of geomagnetic activity and near-earth interplanetary conditions over the past 167 years: 4. Near-earth solar wind speed, IMF, and open solar flux, *Ann. Geophys.*, *32*, 383–399, doi:10.5194/angeo-32-383-2014.

Lui, A. T. Y., R. W. McEntire, and K. B. Baker (2001), A new insight on the cause of magnetic storms, *Geophys. Res. Lett.*, *28*, 3413–3416, doi:10.1029/2001GL013281.

Lyatsky, W., P. T. Newell, and A. Hamza (2001), Solar illumination as the cause of the equinoctial preference for geomagnetic activity, *Geophys. Res. Let.*, *28*, 2353–2356, doi:10.1029/2000GL012803.

Matthaeus, W. H., M. L. Goldstein, and J. H. King (1986), An interplanetary magnetic field ensemble at 1 AU, *J. Geophys. Res.*, *91*, 59–69, doi:10.1029/JA091iA01p00059.

McComas, D. J., J. T. Gosling, S. J. Bame, E. J. Smith, and H. V. Cane (1989), A test of magnetic field draping induced B_z perturbations ahead of fast coronal mass ejecta, *J. Geophys. Res.*, *94*, 1465–1471, doi:10.1029/JA094iA02p01465.

McGranaghan, R., D. J. Knipp, R. L. McPherron, and L. A. Hunt (2014), Impact of equinoctial high-speed stream structures on thermospheric responses, *Space Weather*, *12*, 277–297, doi:10.1002/2014SW001045.

McPherron, R. L., C. T. Russell, and M. Aubry (1973), Satellite studies of magnetospheric substorms on August 15, 1978: 9, Phenomenological model for substorms, *J. Geophys. Res.*, *78*, 3131–3149, doi:10.1029/JA078i016p03131.

McPherron, R. L., G. Siscoe, and C. N. Arge (2004), Probabilistic forecasting of the 3-h *Ap* index, *IEEE Trans. Plasma Sci.*, *32*, 1425–1438, doi:10.1109/TPS.2004.833387.
Miyashita, Y., et al. (2009), A state-of-the-art picture of substorm-associated evolution of the near-Earth magnetotail obtained from superposed epoch analysis, *J. Geophys. Res.*, *114*, A01211, doi:10.1029/2008JA013225.
Moldwin, M. B., S. Ford, R. P. Lepping, J. Slavin, and A. Szabo (2000), Small-scale magnetic flux ropes in the solar wind, *Geophys. Res. Lett.*, *27*, 57–60, doi:10.1029/1999GL010724.
Mulligan, T., C. T. Russell, and J. G. Luhmann (1998), Solar cycle evolution of the structure of magnetic clouds in the inner heliosphere, *Geophys. Res. Lett.*, *25*, 2959–2962, doi:10.1029/98GL01302.
Nishida, A. (1968), Coherence of geomagnetic DP 2 fluctuations with interplanetary magnetic variations, *J. Geophys. Res.*, *73*, 5549–5559, doi:10.1029/JA073i017p05549.
O'Brien, T. P., and R. L. McPherron (2002), Seasonal and diurnal variation of *Dst* dynamics, *J. Geophys. Res.*, *107*(A11), 1341, doi:10.1029/2002JA009435.
Odstrcil, D., V. J. Pizzo, J. A. Linker, P. Riley, R. Lionello, and Z. Mikic (2004a), Initial coupling of coronal and heliospheric numerical magnetohydrodynamic codes, *J. Atmos. Sol. Terr. Phys.*, *66*, 1311–1326, doi:10.1016/j.jastp.2004a.04.007.
Odstrcil, D., P. Riley, and X. P. Zhao (2004b), Numerical simulation of the 12 May 1997 interplanetary CME event, *J. Geophys. Res.*, *109*, A02116, doi:10.1029/2003JA010135.
Owens, M. J., and P. Cargill (2004), Non-radial solar wind flows induced by the motion of interplanetary coronal mass ejections, *Ann. Geophys.*, *22*, 4397–4406, doi:10.5194/angeo-22-4397-2004.
Owens, M. J., and R. J. Forsyth (2013), The heliospheric magnetic field, *Living Rev. Solar Phys.*, *10*, 5, doi:10.12942/lrsp-2013-5.
Owens, M. J., P. J. Cargill, C. Pagel, G. L. Siscoe, and N. U. Crooker (2005), Characteristic magnetic field and speed properties of interplanetary coronal mass ejections and their sheath regions, *J. Geophys. Res.*, *110*, A01105, doi:10.1029/2004JA010814.
Owens, M. J., R. T. Wicks, and T. S. Horbury (2011), Magnetic discontinuities in the near-earth solar wind: Evidence of in-transit turbulence or remnants of coronal structure?, *Sol. Phys.*, *269*(2), 411–420, doi:10.1007/s11207-010-9695-0.
Owens, M. J., N. U. Crooker, and M. Lockwood (2014), Solar cycle evolution of dipolar and pseudostreamer belts and their relation to the slow solar wind, *Geophys. Res. Space Physics*, *119*, 36–46, doi:10.1002/2013JA019412.
Parker, E. N. (1958), Dynamics of the interplanetary gas and magnetic fields, *Astrophys. J.*, *128*, 664–676, doi:10.1086/146579.
Pizzo, V. J. (1978), A three-dimensional model of corotating streams in the solar wind. I—Theoretical foundations, *J. Geophys. Res.*, *83*, 5563–5572, doi:10.1029/JA083iA12p05563.
Reeves, G. D., and M. G. Henderson (2001), The storm-substorm relationship: Ion injections in geosynchronous measurements and composite energetic neutral atom images, *J. Geophys. Res.*, *106*, 5833–5844, doi:10.1029/2000JA003017.
Reeves, G. D., et al. (2003), IMAGE, POLAR, and geosynchronous observations of substorm and ring current ion injection, in *Disturbances in Geospace: The Storm-Substorm Relationship*, edited by A. S. Sharma, Y. Kamide, and G. S. Lakhina, pp. 91–101, AGU, Washington, D. C., doi:10.1029/142GM09.
Richardson, I. G., and H. V. Cane (2010), Near-earth interplanetary coronal mass ejections during solar cycle 23 (1996 – 2009): Catalog and summary of properties, *Sol. Phys.*, *264*, 189–237, doi:10.1007/s11207-010-9568-6.
Richardson, I. G., and H. V. Cane (2012), Solar wind drivers of geomagnetic storms during more than four solar cycles, *J. Space Weather Space Clim.*, *2*, 1–9, doi:10.1051/swsc/2012001.
Richardson, I. G., E. W. Cliver, and H. V. Cane (2001), Sources of geomagnetic storms for solar minimum and maximum conditions during 1972–2000, *Geophys. Res. Lett.*, *28*(13), 2569–2572, doi:10.1029/2001GL013052.
Richardson, I. G., H. V. Cane, and E. W. Cliver (2002), Sources of geomagnetic activity during nearly three solar cycles (1972–2000), *J. Geophys. Res.*, *107*(A8), 1187, doi:10.1029/2001JA000504.
Rosenberg, R. L., and P. J. Coleman (1969), Heliographic latitude dependence of the dominant polarity of the interplanetary magnetic field, *J. Geophys. Res.*, *74*, 5611–5622, doi:10.1029/JA074i024p05611.
Rouillard, A. P., and M. Lockwood (2007), The latitudinal effect of co-rotating interaction regions on galactic cosmic rays, *Solar Phys.*, *245*, 191–206, doi:10.1007/s11207-007-9019-1.
Rouillard, A. P., et al. (2008), First imaging of corotating interaction regions using the STEREO spacecraft, *Geophys. Res. Lett.*, *35*, L10110, doi:10.1029/2008GL033767.
Rouillard, A. P., et al. (2009), A multispacecraft analysis of a small-scale transient entrained by solar wind streams, *Solar Phys.*, *256*, 307–326, doi:10.1007/s11207-009-9329-6.
Rouillard, A. P., et al. (2010a), Intermittent release of small-scale transients in the slow solar wind: I. Remote sensing observations, *J. Geophys. Res.*, *115*, A04103, doi:10.1029/2009JA014471.
Rouillard, A. P., et al. (2010b), Intermittent release of small-scale transients in the slow solar wind: II. In-situ evidence, *J. Geophys. Res.*, *115*, A04104, doi:10.1029/2009JA014472.
Rouillard, A. P., et al. (2011), The solar origin of small interplanetary transients, *Astrophys. J.*, *734*(1), 7/1–7/10, doi:10.1088/0004-637X/734/1/7.
Russell, C. T., and R. L. McPherron (1973), Semiannual variation of geomagnetic activity, *J. Geophys. Res.*, *78*, 82–108, doi:10.1029/JA078i001p00092.
Russell, C. T., Y. L. Wang, and J. Raeder (2003), Possible dipole tilt depedendence of dayside magnetopause reconnection, *Geophys. Res. Lett.*, *30*(18), 1937, doi:10.1029/2003GL017725.
Scott, C. J., R. G. Harrison, M. J. Owens, M. Lockwood, and L. Barnard (2014), Evidence for solar wind modulation of lightning, *Env. Res. Lett.*, *9*, 055004, doi:10.1088/1748-9326/9/5/055004.
Sheeley, N. R., Jr., J. H. Walters, Y.-M. Wang, and R. A. Howard (1999), Continuous tracking of coronal outflows: Two kinds of coronal mass ejections, *J. Geophys. Res.*, *104*, 24,739–24,767, doi:10.1029/1999JA900308.
Sheeley, N. R., D. D.-H. Lee Jr., K. P. Casto, Y.-M. Wang, and N. B. Rich (2009), The structure of streamer blobs, *Astrophys. J.*, *694*, 1471–1480, doi:10.1088/0004-637X/694/2/1471.
Smith, E. J., and J. H. Wolfe (1976), Observations of interaction regions and corotating shocks between one and five AU: Pioneers 10 and 11, *Geophys. Res. Lett.*, *3*, 137–140, doi:10.1029/GL003i003p00137.
Smith, M. F., and M. Lockwood (1996), The Earth's magnetospheric cusps, *Rev. Geophys.*, *34*, 233–260, doi:10.1029/96RG00893.
Stamper, R., M. Lockwood, M. N. Wild, and T. D. G. Clark (1999), Solar causes of the long term increase in geomagnetic activity, *J. Geophys. Res.*, *104*, 28,325–28,342, doi:10.1029/1999JA900311.
Svalgaard, L., E. W. Cliver, and A. G. Ling (2002), The semiannual variation of great geomagnetic storms, *Geophys. Res. Lett.*, *29*(16), 1765, doi:10.1029/2001GL014145.
Takalo, J., and K. Mursula (2001), A model for the diurnal universal time variation of the *Dst* index, *J. Geophys. Res.*, *106*, 10,905–10,913, doi:10.1029/2000JA000231.

Temerin, M., and X. Li (2002), A new model for the prediction of *Dst* on the basis of the solar wind, *J. Geophys. Res.*, *107*(A12), 1472, doi:10.1029/2001JA007532.
Thomas, B. T., and E. J. Smith (1981), The structure and dynamics of the heliospheric current sheet, *J. Geophys. Res.*, *86*, 11,105–11,110, doi:10.1029/JA086iA13p11105.
Thomsen, M. F. (2004), Why *Kp* is such a good measure of magnetospheric convection?, *Space Weather*, *2*, S11004, doi:10.1029/2004SW000089.
Todd, H., S. W. H. Cowley, M. Lockwood, D. M. Willis, and H. Lühr (1988), Response time of the high-latitude dayside ionosphere to sudden changes in the north-south component of the IMF, *Planet. Space Sci.*, *36*, 1415–1428, doi:10.1016/0032-0633(88)90008-6.
Tsurutani, B. T., W. D. Gonzalez, A. L. Clúa de Gonzalez, F. Tang, J. K. Arballo, and M. Okada (1995), Interplanetary origin of geomagnetic activity in the declining phase of the solar cycle, *J. Geophys. Res.*, *100*, 21,717–21,733, doi:10.1029/95JA01476.
Tsurutani, B. T., et al. (2006), Corotating solar wind streams and recurrent geomagnetic activity: A review, *J. Geophys. Res.*, *111*, A07S01, doi:10.1029/2005JA011273.
Turner, D. L., et al. (2015), Energetic electron injections deep into the inner magnetosphere associated with substorm activity, *Geophys. Res. Lett.*, *42*, 2079–2087, doi:10.1002/2015GL063225.
Turner, N. E., W. D. Cramer, S. K. Earles, and B. A. Emery (2009), Geoefficiency and energy partitioning in CIR-driven and CME-driven storms, *J. Atmos. Sol. Terr. Phys.*, *71*, 1023–1031, doi:10.1016/j.jastp.2009.02.005.
Webb, D. F., and R. A. Howard (1994), The solar cycle variation of coronal mass ejections and the solar wind mass flux, *J. Geophys. Res.*, *99*, 4201–4220, doi:10.1029/93JA02742.
Weigel, R. S. (2010), Solar wind density influence on geomagnetic storm intensity, *J. Geophys. Res.*, *115*, A09201, doi:10.1029/2009JA015062.
Xie, H., N. Gopalswamy, O. C. St. Cyr, and S. Yashiro (2008), Effects of solar wind dynamic pressure and preconditioning on large geomagnetic storms, *Geophys. Res. Lett.*, *35*, L06S08, doi:10.1029/2007GL032298.
Xu, D., T. Chen, X. X. Zhang, and Z. Liu (2009), Statistical relationship between solar wind conditions and geomagnetic storms in1998–2008, *Planet. Space Sci.*, *57*(12), 1500–1513, doi:10.1016/j.pss.2009.07.015.
Yashiro, S., N. Gopalswamy, G. Michalek, O. C. St. Cyr, S. P. Plunkett, N. B. Rich, and R. A. Howard (2004), A catalog of white light coronal mass ejections observed by the SOHO spacecraft, *J. Geophys. Res.*, *109*, A07105, doi:10.1029/2003JA010282.
Yermolaev, Y. I., N. S. Nikolaeva, I. G. Lodkina, and M. Y. Yermolaev (2012), Geoeffectiveness and efficiency of CIR, sheath, and ICME in generation of magnetic storms, *J. Geophys. Res.*, *117*, A00L07, doi:10.1029/2011JA017139.
Yu, W., et al. (2014), A statistical analysis of properties of small transients in the solar wind 2007–2009: STEREO and Wind observations, *J. Geophys. Res. Space Physics*, *119*, 689–708, doi:10.1002/2013JA019115.
Zhang, J.-C., M. W. Liemohn, J. U. Kozyra, M. F. Thomsen, H. A. Elliott, and J. M. Weygand (2006), A statistical comparison of solar wind sources of moderate and intense geomagnetic storms at solar minimum and maximum, *J. Geophys. Res.*, *111*, A01104, doi:10.1029/2005JA011065.
Zhang, Q.-H., et al. (2013), Direct observations of the evolution of polar cap ionization patches, *Science*, *339*, 1597–1600, doi:10.1123/science.1231487.
Zhang, Q.-H., M. Lockwood, J. C. Foster, S.-R. Zhang, B.-C. Zhang, I. W. McCrea, J. Moen, M. Lester, and J. M. Ruohoniemi (2015), Direct observations of the full Dungey convection cycle in the polar ionosphere for southward interplanetary magnetic field conditions, *J. Geophys. Res. Space Physics*, *120*, 4519–4530, doi:10.1002/2015JA021172.
Zhao, H., and Q.-G. Zong (2012), Seasonal and diurnal variation of geomagnetic activity: Russell-McPherron effect during different IMF polarity and/or extreme solar wind conditions, *J. Geophys. Res.*, *117*, A11222, doi:10.1029/2012JA017845.